



21

## Abstract

22 Membrane separation and advanced oxidation processes (AOPs) have been respectively  
23 demonstrated to be effective for a variety of water and/or wastewater treatments. Innovative  
24 integration of membrane with catalytic oxidation is thus expected to be more competing for  
25 more versatile applications. In this study, ceramic membranes (CMs) integrated with  
26 manganese oxide ( $\text{MnO}_2$ ) were designed and fabricated via a simple one-step ball-milling  
27 method with a high temperature sintering. Functional membranes with different loadings of  
28  $\text{MnO}_2$  (1.67%, 3.33% and 6.67% of the total membrane mass) were then fabricated. The micro-  
29 structures and compositions of the catalytic membranes were investigated by a number of  
30 advanced characterisations. It was found that the  $\text{MnO}_2$  nanocatalysts (10-20 nm) were  
31 distributed uniformly around the  $\text{Al}_2\text{O}_3$  particles (500 nm) of the membrane basal material, and  
32 can provide a large amount of active sites for the peroxymonosulfate (PMS) activation which  
33 can be facilitated within the pores of the catalytic membrane. The catalytic degradation of 4-  
34 hydroxybenzoic acid (HBA), which is induced by the sulfate radicals via PMS activation, was  
35 investigated in a cross-flow membrane unit. The degradation efficiency slightly increased with  
36 a higher  $\text{MnO}_2$  loading. Moreover, even with the lowest loading of  $\text{MnO}_2$  (1.67%), the  
37 effectiveness of HBA degradation was still prominent, shown by that a 98.9 % HBA  
38 degradation was achieved at the permeated side within 30 min when the initial HBA  
39 concentration was 80 ppm. The stability and leaching tests revealed a good stability of the  
40 catalytic membrane even after the 6<sup>th</sup> run. Electron paramagnetic resonance (EPR) and  
41 quenching tests were used to investigate the mechanism of PMS activation and HBA  
42 degradation. Both sulfate radicals ( $\text{SO}_4^{\cdot-}$ ) and hydroxyl radicals ( $\cdot\text{OH}$ ) were generated in the  
43 catalytic membrane process. Moreover, the contribution from non-radical process was also  
44 observed. This study provides a novel strategy for preparing a ceramic membrane with the

45 function of catalytic degradation of organic pollutants, as well as outlining into future  
46 integration of separation and AOPs.

47 **Keywords:** Manganese oxides; Catalytic membrane; Sulfate radicals; 4-hydroxylbenzoic acid  
48 (HBA); AOPs.

49

## 50 **1. Introduction**

51 Aqueous organics pollution is one of the most serious environmental issues, and has drawn  
52 increasing public concerns. Organic contaminants, for example, hydrocarbons, detergents,  
53 pharmaceutical compounds, pesticides, surfactants and dyes, are recalcitrant to natural  
54 degradation, therefore have caused various problems related to water shortage and public health  
55 risks (Sun and Wang 2015). This leads to the development of a variety of water treatment  
56 technologies, for instance, adsorption, flocculation, biodegradation, and advanced oxidation  
57 processes (AOPs) (Duan et al. 2018c). Different from other technologies, AOPs are generally  
58 conducted with the presence of strong oxidizing species, for example, hydroxyl ( $\cdot\text{OH}$ ), sulfate  
59 ( $\text{SO}_4^{\cdot-}$ ), and superoxide radicals ( $\text{O}_2^{\cdot-}$ ), which are produced *in situ* through photocatalysis,  
60 electrochemistry, or activation of superoxides (hydrogen peroxide, ozone, and persulfate, etc.).  
61 The reactive radicals can trigger a sequence of reactions that decompose the organic  
62 compounds into smaller and less harmful substances (Chan et al. 2011, (Duan et al. 2018c).  
63 For example, Fenton reaction is a classical AOP, which relies on the reactions between  
64 Fenton's reagents, e.g., hydrogen peroxide ( $\text{H}_2\text{O}_2$ ) and ferrous ions, to generate hydroxyl  
65 radicals ( $\cdot\text{OH}$ ). However, the Fenton's reaction prefers an acidic environment ( $\text{pH} < 3$ ), which  
66 requires the extra controls of the solution, including reducing the solution pH value before the  
67 treatment, and neutralizing after the reactions. Furthermore, there are associated drawbacks

68 that cannot be ignored, such as the large amount of sludge produced, as well as the difficulties  
69 in storing and using H<sub>2</sub>O<sub>2</sub> (Neyens and Baeyens 2003, (Sun and Wang 2015).

70 As an alternative to hydroxyl radicals ( $\cdot\text{OH}$ ), sulfate radicals ( $\text{SO}_4^{\cdot-}$ ) have the merits of a higher  
71 oxidative potential (2.5- 3.1 V at neutral pH vs 1.8-2.7 V of hydroxyl radicals), a relative non-  
72 selectivity, a longer lifetime, and good activity across a wide range of pH values (Sun and  
73 Wang 2015). Because of the advantages of sulfate radicals, the sulfate radical-based advanced  
74 oxidation processes (SR-AOPs) have broad applications in removing refractory organic  
75 pollutants (Xia et al. 2017, (Yin et al. 2019), microorganisms (Wang et al. 2019) and  
76 microplastic (MPs) (Kang et al. 2019b). Sulfate radicals can be generated via the activation of  
77 either peroxymonosulfate ( $\text{HSO}_5^-$ , PMS) or persulfate ( $\text{S}_2\text{O}_8^{2-}$ , PS). The asymmetric structure  
78 ( $\text{HO-O-SO}_3^-$ ) and longer superoxide O-O bond ( $l_{\text{o-o}}=1.326 \text{ \AA}$ ) make PMS easier be dissociated  
79 than PS, since PS has a symmetric structure ( $\text{SO}_3^- \text{-O-O-SO}_3^-$ ) and a more compact O-O bond  
80 ( $l_{\text{o-o}}=1.322 \text{ \AA}$ ) (Duan et al. 2018b). Persulfate salts (PMS and PS) are hard to decompose  
81 naturally, thus a catalyst is usually required to activate persulfate salts (PMS and PS) to  
82 accelerate the process of producing sulfate radicals ( $\text{SO}_4^{\cdot-}$ ). Similar to H<sub>2</sub>O<sub>2</sub> and O<sub>3</sub> that are  
83 commonly used in other AOPs, PMS and PS can be activated either homogeneously with metal  
84 ions (Anipsitakis and Dionysiou 2003, (Anipsitakis and Dionysiou 2004a, b) or  
85 heterogeneously with metal oxides/metal-free carbons. Compared with homogeneous  
86 activation, heterogeneous activation by catalysts can avoid the severe loss of metal ions. Metal  
87 based-catalysts such as manganese oxides (Saputra et al. 2013a, (Saputra et al. 2013b, (Saputra  
88 et al. 2013c, (Wang et al. 2015a), cobalt oxides (Saputra et al. 2013a, (Wang et al. 2015c) and  
89 zero valence iron (Sun et al. 2012, (Wang et al. 2015b), were found to be very effective in the  
90 activation of PMS/PS. Although the effectiveness of metal-based catalysts has been verified,  
91 the potential leaching of toxic transition metals into water system is a serious issue resulting in  
92 secondary contamination to environment. As a promising alternative, metal-free nanocarbons

93 and carbonaceous catalysts have been proven to be an inexpensive and environmental-friendly  
94 choice for SR-AOPs. Great works have been done and a variety of novel metal-free catalysts  
95 such as reduced graphene oxide (rGO) (Duan et al. 2015a, (Duan et al. 2016b, (Duan et al.  
96 2018c, (Kang et al. 2016), carbon nanotubes (CNTs) (Duan et al. 2018c, (Kang et al. 2019a,  
97 (Sun et al. 2014), and cubic mesoporous carbon (CMK) (Duan et al. 2018c, (Duan et al. 2018d)  
98 were synthesized for achieving the sulfate radicals ( $\text{SO}_4^{\cdot-}$ ) generation. Along with the SR-  
99 AOPs, two possible pathways, e.g. radical and nonradical degradation, have been proposed  
100 (Duan et al. 2018a, (Duan et al. 2016a, (Duan et al. 2018c).

101 A major problem of SR-AOPs with homogeneous/heterogeneous catalysis is the recovery and  
102 reuse of the catalysts. Catalytic membrane is thus a promising solution by combining  
103 membrane separation of catalysts, and catalytic decomposition of the organic pollutants via  
104 radicals. The studies on photocatalytic membranes (Wang et al. 2017b, (Zhao et al. 2016) and  
105 ozonation membranes (Chen et al. 2015, (Guo et al. 2016) revealed the competing  
106 performances in the treatments of aqueous organic pollutants. Recently, integrated membrane  
107 with sulfate radicals ( $\text{SO}_4^{\cdot-}$ ) based-catalytic oxidation has attracted increasing attention. Cheng  
108 et al. studied ferrous iron/peroxymonosulfate (Fe (II)/PMS) oxidation process as a pre-  
109 treatment method for fouling alleviation on ultrafiltration (UF) ceramic membrane caused by  
110 natural organic matters (NOMs). It was found that the sulfate radicals in Fe (II)/PMS oxidation  
111 process were very effective both in the removal of atrazine (ATZ) (98.2% ATZ removal with  
112 Fe (II)/PMS at 50/50  $\mu\text{M}$ ), and the mitigation of membrane fouling caused by humic acid (HA),  
113 sodium alginate (SA), bovine serum albumin (BSA), and their mixture (HA-BA-BSA) (Cheng  
114 et al. 2017). In another work, the anti-fouling performance for algal extracellular organic  
115 matters (EOMs) was investigated, and it was found that UV/Fe(II)/PMS process showed the  
116 best anti-fouling performance (Cheng et al. 2018). Bao et al. prepared  $\text{CoFe}_2\text{O}_4$  nanocatalysts  
117 impregnated  $\text{Al}_2\text{O}_3$  ceramic membrane via the urea-assisted one-step combustion method.

118 Nearly 100% sulfamethoxazole (SMX, initial concentration of 10 ppm) was removed within  
119 90 s. The effects of Oxone loading, humic acid (HA) concentration and anions ( $\text{CO}_3^{2-}$ ,  $\text{SO}_4^{2-}$ ,  
120  $\text{NO}_3^-$ , and  $\text{Cl}^-$ ) on degradation efficiencies were also investigated (Bao et al. 2018). Luo et al.  
121 synthesized a free-standing glass fibre supported hierarchical  $\alpha\text{-MnO}_2\text{@CuO}$  membrane for  
122 organic dye removal. Fast degradation of methyl blue (MB) was achieved within 0.23 s of the  
123 residence time when the solution flow rate was controlled at 20 mL/min. The mechanistic study  
124 was conducted by electron paramagnetic resonance (EPR) and quenching tests. Both sulfate  
125 radicals ( $\text{SO}_4^{\cdot-}$ ) and hydroxyl radicals ( $\cdot\text{OH}$ ) were produced from the interaction between PMS  
126 and  $\alpha\text{-MnO}_2\text{@CuO}$  catalytic membrane (Luo et al. 2018). Zhao et al. fabricated different metal  
127 oxides ( $\text{MnO}_2$ ,  $\text{Fe}_2\text{O}_3$ ,  $\text{Co}_3\text{O}_4$ ,  $\text{CuO}$  and  $\text{Mn}_3\text{O}_4$ ) coated ceramic membranes (CMs) and  
128 compared their performances for cleaning foulants with the assistance of PMS. The  $\text{MnO}_2$ -  
129 coated CM showed the best performance of flux recovery after the cleaning using PMS solution  
130 (Zhao et al. 2019). In addition, the  $\text{MnO}_2$  and  $\text{Co}_3\text{O}_4$  are the most popular metal-based catalysts  
131 for heterogeneous activation of PMS. It was suggested that  $\text{MnO}_2$  might be better than cobalt  
132 oxides for wider applications in SR-AOPs because of the abundance of  $\text{MnO}_2$  in nature and its  
133 relatively lower toxicity to water bodies. It was reported that the  $\text{LC}_{50}$  (metal concentrations in  
134 water resulting in 50% mortality in 4 weeks) of cobalt and manganese are 183 and 197,000  
135  $\text{nmol L}^{-1}$ , respectively (Norwood et al. 2007).

136 Herein, we report a  $\text{MnO}_2$  integrated ceramic membrane prepared via a simple one-step ball-  
137 milling with high temperature sintering method. To the best of our knowledge, this is the first  
138 study on loading  $\text{MnO}_2$  nanoparticles uniformly into the pores and surface of a ceramic  
139 membrane for AOPs. Compared with other AOPs based-catalytic membranes, our catalytic  
140 ceramic membranes showed an outstanding performance in degrading the antibiotic pollutant  
141 of 4-hydroxybenzoic acid (4-HBA), even at a very high initial concentration (80 ppm), because  
142 of the dispersive distribution of very fine  $\text{MnO}_2$  nanoparticles (10-20 nm) within the pores and

143 on the surface of the membrane. In addition, unlike the polymeric supports, the alumina  
144 ceramic membrane support provides a high stability for the catalytic oxidation reactions. The  
145 reusability tests showed no significant decrease in the degradation performance of HBA after  
146 the 6<sup>th</sup> run. The one-step ball-milling preparation method in this study makes the catalytic  
147 membrane feasible for practical applications at a large scale.

148

## 149 **2. Experimental**

### 150 2.1. Reagents and materials

151 In the study, 4-hydroxybenzoic acid (4-HBA), Oxone (PMS, 2KHSO<sub>5</sub>·KHSO<sub>4</sub>·K<sub>2</sub>SO<sub>4</sub>), acetic  
152 acid (CH<sub>3</sub>COOH), hydrochloric acid (HCl), polyvinyl alcohol ((C<sub>2</sub>H<sub>4</sub>O)<sub>x</sub>, PVA), methanol  
153 (CH<sub>4</sub>O), *tert*-butanol (TBA), ethanol (C<sub>2</sub>H<sub>5</sub>OH) and 5, 5-dimethyl-1-pyrrolidine N-oxide  
154 (DMPO) were purchased from Sigma-Aldrich. Potassium permanganate (KMnO<sub>4</sub>) was  
155 supplied by Chem-Supply. Glycerol (C<sub>3</sub>H<sub>8</sub>O<sub>3</sub>) was obtained from Rowe-Scientific. Al<sub>2</sub>O<sub>3</sub>  
156 nanoparticles (corundum, 500 nm) were purchased from NanoAmor. Grinding balls  
157 (Zirconium, 1, 2, 5, 10 and 20 MM diameters) were supplied by Nikkato. All solutions were  
158 prepared using ultrapure water (18.2 MΩ.cm at 25 °C) from a Mill-Q water system. All  
159 chemicals were used as received without further purification.

### 160 2.2. Synthesis of MnO<sub>2</sub> catalysts

161 Spherically structured MnO<sub>2</sub> was prepared by a modified hydrothermal process, via the  
162 reduction of KMnO<sub>4</sub> reported in our previous studies (Wang et al. 2015a). The amount of HCl  
163 was modified in order to obtain uniform MnO<sub>2</sub> of the desired nanostructure. In a typical  
164 synthesis, 2.85 mM of KMnO<sub>4</sub> was first dissolved in 80 mL of ultrapure water. Then 2 mL of  
165 HCl (37 wt%) was added to the solution drop wisely under vigorous magnetic stirring to form

166 the precursor solution. After stirring for about 20 min, the solution was transferred into a 120  
167 mL Teflon-lined stainless steel autoclave. The autoclave was then heated in an electric oven to  
168 110 °C for 12 h. The autoclave was then naturally cooled down to room temperature. The black  
169 precipitate was then collected by vacuum filtration, followed by washing with deionized water  
170 and ethanol for 3 times and then dried at 60 °C overnight.

### 171 2.3. Preparation of manganese oxide-integrated ceramic membranes

172 MnO<sub>2</sub> integrated CM discs (3.5 g each) were prepared by the following route: a certain amount  
173 of MnO<sub>2</sub>, PVA (1 %), glycerol (1.5 %) and Al<sub>2</sub>O<sub>3</sub> were first mixed together and put into the  
174 ZrO<sub>2</sub> ball-milling bowl (500 mL in volume, Fritsch, Germany), where the MnO<sub>2</sub> loading was  
175 set to 1.67%, 3.33%, and 6.67% of the total mass of membrane samples which were then  
176 denoted to Mn-1/Al, Mn-3/Al, and Mn-6/Al, respectively. A planetary ball-mill (Fritsch,  
177 Pulverisette 6, Germany) was utilised to mix the membrane contents, in which the grinding  
178 balls were a mixture of Nikkato ZrO<sub>2</sub> balls in the diameters of 1, 2, 5, 10, and 20 mm. The mass  
179 ratio of powders to balls was set at 1/10. Then the after-milling powders were transferred to an  
180 automatic sieve shaker (Retsch, AS 200 Control, Germany) to obtain uniform fine powder  
181 mixture. The sieved powders were then transferred to a disc mould and pressed under the  
182 pressure of 5 bar by a hydraulic press (Specac, UK) to produce the green-pressing membranes.  
183 After dried at 60 °C in the oven overnight, the green-pressing membranes were sintered in a  
184 high temperature muffle furnace at 1050 °C to obtain the final membranes (28 mm in diameter  
185 size and 3.5 mm in thickness). In addition, the pure alumina ceramic membrane supports were  
186 made by the same procedure without the addition of any manganese oxides when ball-milling.  
187 The photos of the pure alumina ceramic membrane support and Mn-1, Mn-3 and Mn-6  
188 membranes are shown in Fig. S1 (a), and the size of membrane disc is displayed in Fig. S1 (b)  
189 and (c).

190

#### 191 2.4. Characterization

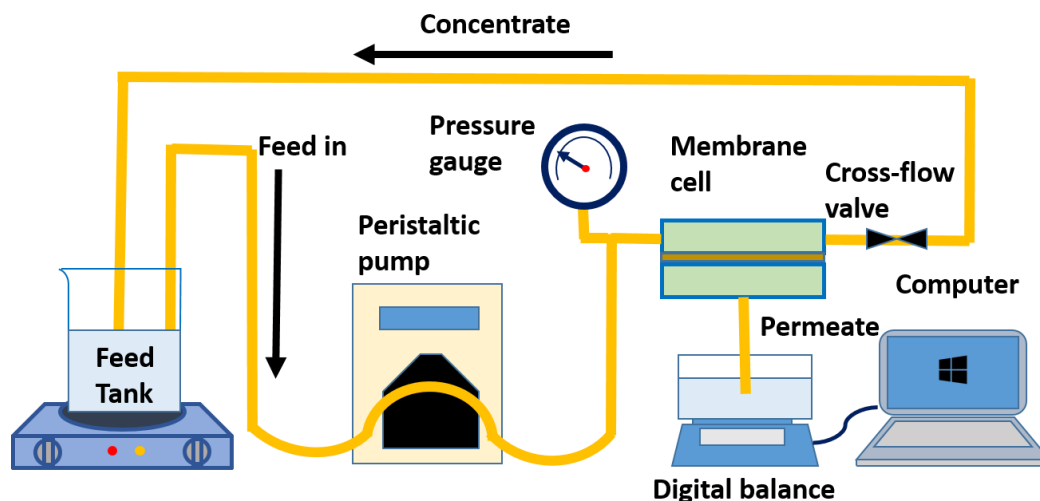
192 The surface morphologies and energy dispersive spectrometry (EDS) element mappings of the  
193 catalytic membranes were characterised by scanning electron microscopy (SEM, Zeiss 1555,  
194 Germany). The morphologies and lattice spacing of manganese oxide catalysts within alumina  
195 aggregates were investigated by a high resolution transmission electron microscopy (HRTEM,  
196 Thermo FEI Titan G2 80-200, US). The components and structures of ceramic membranes  
197 were investigated by X-ray diffraction (XRD, Bruker D8 diffractometer, Germany) using  
198 filtered Cu K $\alpha$  radiation ( $\lambda = 1.5418 \text{ \AA}$ ) with an accelerating voltage of 40 kV and a current of  
199 30 mA. X-ray photoelectron spectroscopy (XPS) was used to determine the chemical states of  
200 elements on a Thermo Escalab 250 (Thermo Fisher Scientific, US) with Al-K $\alpha$  X-ray. Electron  
201 paramagnetic resonance (EPR) spectra were obtained on a Bruker EMS-plus to detect the free  
202 radicals generated during PMS activation. Mn ions were detected by a 4200 MP-AES system  
203 (Agilent, US).

#### 204 2.5. Membrane catalytic oxidation tests

205 The performance of the MnO<sub>2</sub>/Al<sub>2</sub>O<sub>3</sub> membrane was tested in a laboratory-scale SR-AOPs  
206 catalytic membrane system (Fig. 1). Membrane was fixed in a cross-flow membrane module.  
207 A peristaltic pump was used to drive the feed solution and circulate it back to the feed tank. 4-  
208 hydroxybenzoic acid (HBA) was selected as the target pollutant to investigate the ability of  
209 antibiotic pollutants removal on the MnO<sub>2</sub>/Al<sub>2</sub>O<sub>3</sub> via PMS activation. In comparison, different  
210 manganese loading of MnO<sub>2</sub>/Al<sub>2</sub>O<sub>3</sub> (1.67%, 3.33% and 6.67% wt % MnO<sub>2</sub> in Al<sub>2</sub>O<sub>3</sub> of Mn-  
211 1/Al, Mn-3/Al and Mn-6/Al, respectively) catalytic membranes and pure Al<sub>2</sub>O<sub>3</sub> membrane  
212 under the same condition were carried out in the same membrane unit. Unless stated otherwise,  
213 the flow rate was kept at 0.2 mL/min, and the transmembrane pressure (TMP) was controlled

214 at 2 bar. HBA concentrations of feed and filtrate were monitored by an ultra-high performance  
215 liquid chromatography (UHPLC, Shimadzu Prominence, Japan) with a column (Restek Raptor  
216 C18, 2.7  $\mu\text{m}$ , 100  $\times$  2.1 mm, France). The solvent used in the UHPLC was water (pH adjusted  
217 by acetic acid at 3.5): methanol in the ratio of 90:10, with the flow rate was set at 0.3 mL/min.  
218 The column oven was set at 30  $^{\circ}\text{C}$  and the detector wavelength was 270 nm. At certain time  
219 intervals, 1 mL solution was extracted from both permeate side and feed side. Then 1 mL  
220 sample solution was transferred into a 1.5 mL HPLC vial which contained pre-injected 0.5 mL  
221 methanol as the quenching agent.

222 The intermediates of HBA degradation were identified by a GC-MS (Agilent 7890B/5977B,  
223 Agilent, USA). The GC-MS was equipped with a DB-17MS column (30 m  $\times$  0.25 mm  $\times$  0.25  
224  $\mu\text{m}$ ) with ultrahigh purity helium (99.999%, BOC, Australia) as the carrier gas at a flow rate  
225 of 1.0 mL  $\text{min}^{-1}$ . The concentrated reaction mixture was initially in the aqueous form, which  
226 was mixed with ethyl acetate in order to extract the organic compounds from aqueous to  
227 organic phase and further, taken into GC-MS analysis. The sample pretreatment procedures  
228 are as follows: at certain time intervals 2 mL solution from permeate side was transferred to a  
229 centrifuge tube, then 2 mL extraction organic solvent ethyl acetate was added in the centrifuge  
230 tube. Then the solution was mixed in a vortex mixer (VELP Scientifica, US) at 2,000 rpm for  
231 60 s and followed by 10 min centrifugation at 9,000 rpm in a lab centrifuge (Sigma, US). The  
232 ramp of the analysis was as follows: initial column temperature was held for 1 min at 80  $^{\circ}\text{C}$ ,  
233 ramped at 5  $^{\circ}\text{C}/\text{min}$  to 120  $^{\circ}\text{C}$  and then immediately ramped at 10  $^{\circ}\text{C}/\text{min}$  to 240  $^{\circ}\text{C}$ . Then the  
234 analysis was immediately ramped at 240 to 280  $^{\circ}\text{C}$  holding for 5 min at the same temperature.  
235 The sample was injected in the splitless mode and the MS analysis was carried out with 70 eV  
236 as ionization energy, 6 kV accelerated voltage and 1,000 as resolving power with solvent delay  
237 (3 min). The inject temperature was set as 280  $^{\circ}\text{C}$ . MS source was set at 230 and MS quad set  
238 at 150  $^{\circ}\text{C}$ . Full scan model ( $m/z= 50-550$ ) was used.



239

240

**Fig. 1.** Process flow diagram of catalytic membrane filtration system.

241

## 2.6. Membrane fouling control analysis

242

The flux changes of the pristine alumina ( $\text{Al}_2\text{O}_3$ ) ceramic membrane and the manganese oxide

243

( $\text{MnO}_2$ )-based catalytic membranes with different Mn loading (Mn-1, Mn-3 and Mn-6) were

244

tested in a dead-end filtration cell. The transmembrane pressure (TMP) was kept at 1 bar

245

through a nitrogen cylinder connected with the filtration cell. During the filtration tests, the

246

permeate flux was monitored by an electronic balance (Kern KB 3600-2N, Germany)

247

connected with computer and the output data were periodically recorded. To measure the pure

248

water permeate flux ( $J_0$ ), ultrapure water was filtered under a pressure of 1 bar during a 30 min

249

filtration period and the average flux was decided as  $J_0$ . To measure the fouling resistance

250

towards humic acid of the  $\text{MnO}_2$  based catalytic membranes (Mn-1, Mn-3 and Mn-6) and the

251

pristine ceramic membrane, a mixture solution (100 mL) of HA (2 g/L) and PMS (4 g/L) was

252

stirred for 30 min at 200 rpm. After that, the pretreated solution samples were immediately

253

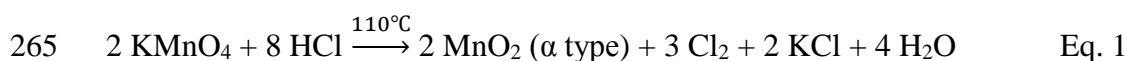
used for membrane filtration.

254

### 255 3. Results

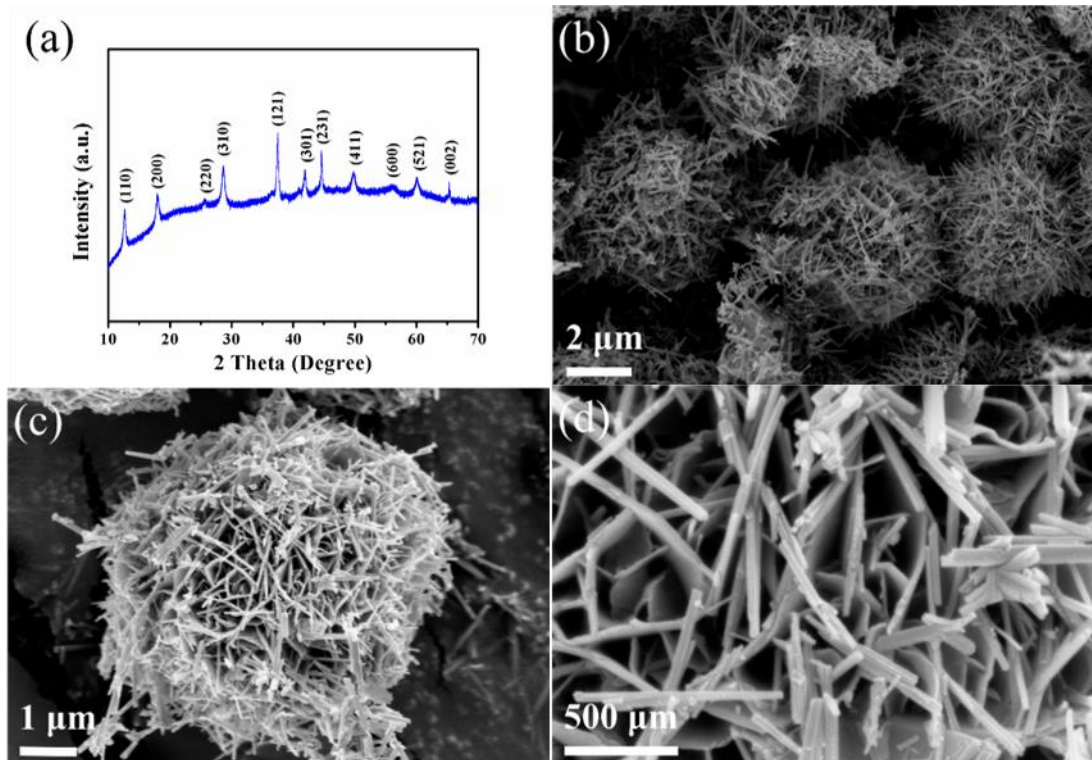
#### 256 3.1. Characterisation of MnO<sub>2</sub> catalysts

257 The crystalline structure of  $\alpha$ -MnO<sub>2</sub> nanostructure was investigated by X-ray diffraction (XRD)  
258 (Fig.2a). Diffraction peaks at  $2\theta$  of 12.7, 18.0, 25.6, 28.7, 37.6, 42.0, 46.1, 49.9, 56.1, 60.2, and  
259 65.5 ° were observed, corresponding to (110), (200), (220), (310), (121), (301), (231), (411),  
260 (600), (521), and (002), respectively. The XRD pattern of manganese oxide was identified to  
261  $\alpha$ -MnO<sub>2</sub> (JCPDS No.72-1982, tetragonal,  $a = b = 9.815 \text{ \AA}$ ,  $c = 2.847 \text{ \AA}$ ) (Wang et al. 2015a).  
262 No other crystalline phase was observed in the pattern, indicating the high purity of the catalyst.  
263 The reaction involved in the hydrothermal process for MnO<sub>2</sub> formation can be described in Eq.  
264 1:



266 Figs. 2 b-d show the SEM images of the structure and morphology of the synthesised MnO<sub>2</sub>  
267 catalysts. After the hydrothermal process at 110 °C, the hollow sea-urchin shaped MnO<sub>2</sub>  
268 catalysts with a diameter of around 5  $\mu\text{m}$  (Figs. 2b-c) were synthesised. The sea-urchin shaped  
269 MnO<sub>2</sub> were made of hollow nanorods with a diameter of about 40 nm (Fig. 2d). The  
270 supplementary images of MnO<sub>2</sub> catalysts and MnO<sub>2</sub>/Al<sub>2</sub>O<sub>3</sub> mixture after ball-milling are shown  
271 in Fig. S2. From Figs. S2a and b, we can further confirm the uniform, spherical MnO<sub>2</sub>  
272 nanoparticles with a diameter of 5  $\mu\text{m}$ . Figs. S2c-f show that after ball-milling, the MnO<sub>2</sub>  
273 nanospheres stucked with Al<sub>2</sub>O<sub>3</sub>, and some MnO<sub>2</sub> catalysts were wrapped by Al<sub>2</sub>O<sub>3</sub>  
274 nanoparticles. The morphologies of MnO<sub>2</sub> heated at different temperatures are shown in Fig.  
275 S3. Figs. S3a and b reveal the SEM images of pristine MnO<sub>2</sub> after the 110 °C hydrothermal  
276 process. It was found that the sea-urchin shaped MnO<sub>2</sub> were made of hollow nanorods. When  
277 the MnO<sub>2</sub> catalysts were heated at 300 °C, the structure and morphology were still maintained.

278 When the heating temperature further rose up to 700 °C, the sea-urchin structure transferred to  
279 an irregular structure with a diameter of 2 to 5 μm. The hollow nanorods structure largely  
280 disappeared but can be still clearly seen at some part of nanorods. Further increasing the  
281 temperature to 1050 °C (equal to the membrane calcination temperature), all particles showed  
282 an irregular structure and the nanorods morphology completely disappeared.



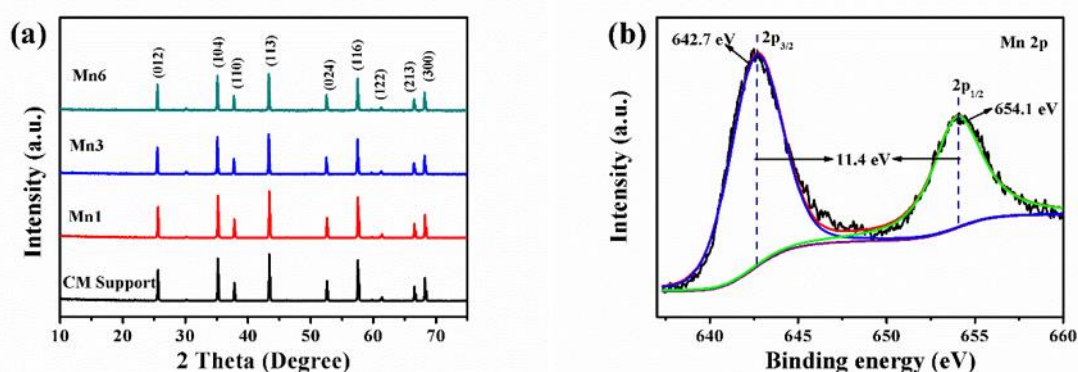
283

284 **Fig. 2.** (a) XRD pattern of MnO<sub>2</sub> catalysts; (b-d) SEM images of MnO<sub>2</sub> catalysts.

### 285 3.2. Properties of MnO<sub>2</sub> integrated ceramic membranes

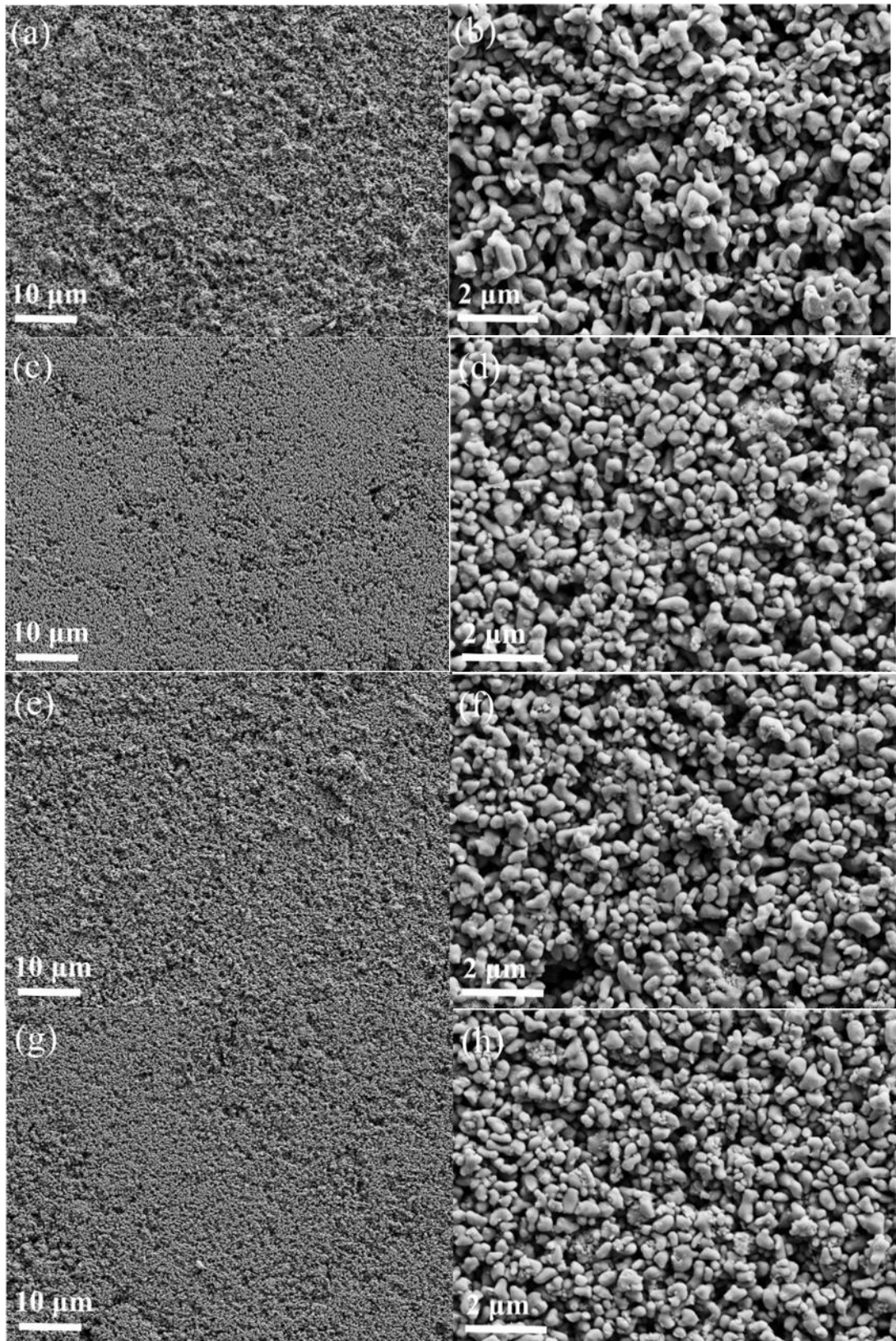
286 Fig. 3a shows XRD patterns of Mn-1/Al, Mn-3/Al, Mn-6/Al catalytic membranes and the pure  
287 Al<sub>2</sub>O<sub>3</sub> membrane. Diffraction peaks at 25.6, 35.2, 37.9, 43.4, 52.7, 57.6, 61.3, 66.7, and 68.4°  
288 were observed, corresponding to (012), (104), (110), (113), (024), (116), (122), (214), and  
289 (300), respectively. The XRD patterns of all the membranes were identified to Al<sub>2</sub>O<sub>3</sub> (JCPDS  
290 No.71-1125, corundum, a = b = 4.748 Å, c = 12.954 Å, α = β = 90°, γ = 120°). No MnO<sub>2</sub>  
291 diffraction peaks were observed, which may be because that the MnO<sub>2</sub> loading is low with a

292 high dispersion degree (Guo et al. 2016). XPS analysis of the pristine membrane and MnO<sub>2</sub>  
 293 integrated catalytic membranes was carried out to unveil the chemical states of manganese (Fig.  
 294 3 b and Figs. S4-7). As shown in Figs. S 4-6, four main elements namely Mn, Al, O, and Zr,  
 295 were observed in the XPS survey spectrum. Zr was from the zirconium oxide (ZrO<sub>2</sub>) grinding  
 296 bowl and grinding balls. Besides them, C element was due to the ingredients of PVA and  
 297 glycerol during the membrane preparation. Al, O, and Mn were the target elements in the Mn-  
 298 1/Al catalytic membrane. The high resolution Mn 2p spectrum (Fig.3b) shows a Mn2p<sub>1/2</sub> peak  
 299 at 654.1 eV and a Mn 2p<sub>3/2</sub> peak at 642.7 eV. The binding energies of Mn 2p with a spin-energy  
 300 separation of 11.4 eV are in accordance with the previous results for MnO<sub>2</sub> (Kim et al. 2013,  
 301 (Wang et al. 2013, (Xiao et al. 2014).



302  
 303 **Fig. 3.** (a) XRD patterns of the membranes: uncoated ceramic membrane, Mn-1/Al, Mn-3/Al,  
 304 and Mn-6/Al catalytic membranes; and (b) Mn 2p spectrum of Mn-1/Al catalytic membrane.

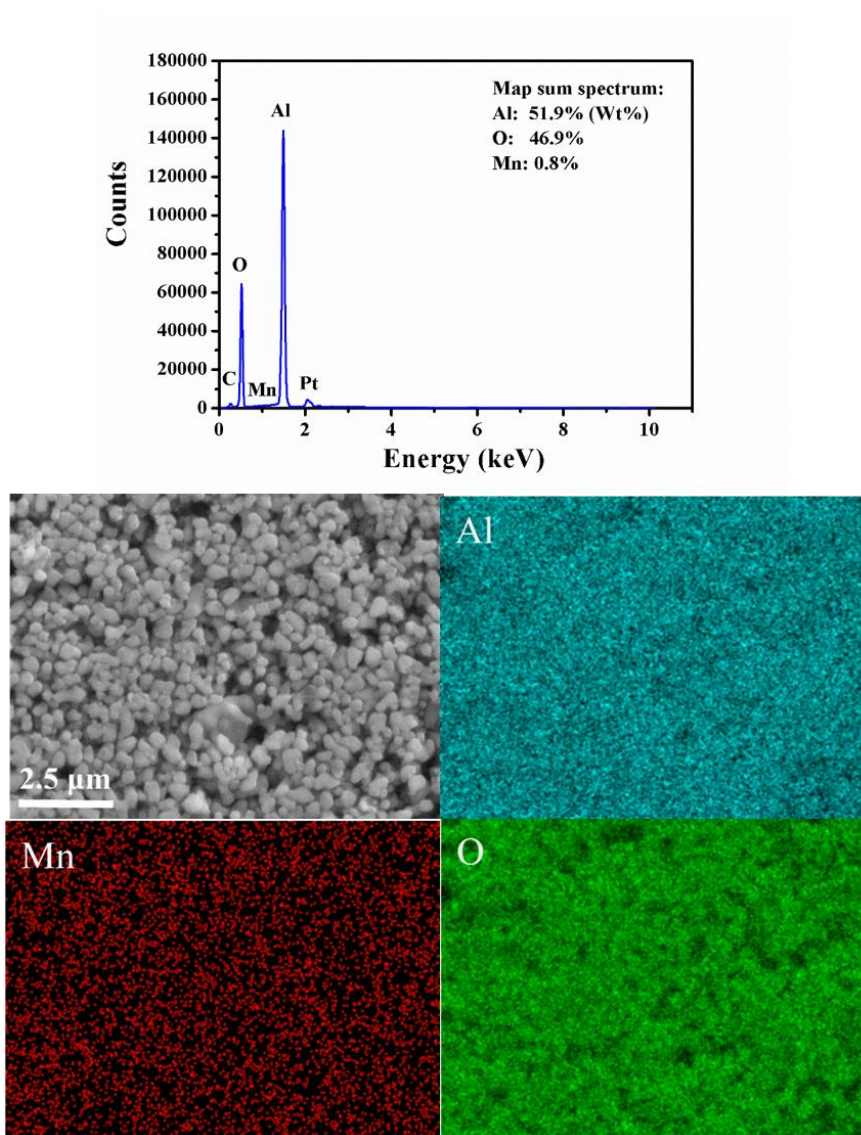
305  
 306 The morphologies of the prepared membranes are presented in Fig.4. In Figs. 4a and b, the  
 307 Al<sub>2</sub>O<sub>3</sub> membrane support shows the particle size ranging from 300 to 500 nm. The surface  
 308 morphologies of Mn-1/Al, Mn-3/Al, and Mn-6/Al membrane are displayed in Figs. 4c and d,  
 309 e and f, and g and h, respectively.



310

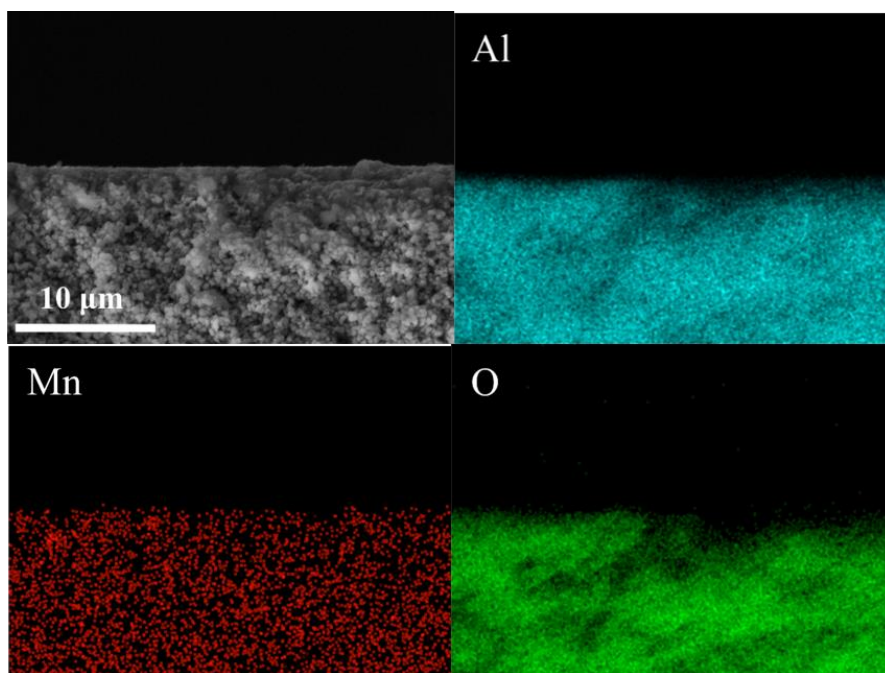
311 **Fig. 4.** SEM images of the ceramic membranes (surface): (a), (b) pristine ceramic membrane,  
312 (c), (d) Mn-1/Al catalytic membrane, (e), (f) Mn-3/Al catalytic membrane, and (g), (h) Mn-  
313 6/Al catalytic membrane.

314 Microanalysis of EDS surface mapping was performed on the Al<sub>2</sub>O<sub>3</sub> membrane and the  
315 modified Mn-1/Al, Mn-3/Al and Mn-6/Al membranes. The EDS mapping of the uncoated (Fig.  
316 S8) and different loaded catalytic membranes (Fig. 5, Fig. S8, and Fig. S9) indicate that the  
317 uniformly-distributed MnO<sub>2</sub> fine particles are integrated by the membrane. This can be further  
318 confirmed by the cross-sectional SEM-EDS mapping (Fig. 6). The element spectra of uncoated  
319 catalytic membranes with different loading are also shown in Fig.5, and Figs. S 8-10, wherein  
320 manganese can be confirmed. And from the quantitative analysis of area EDS spectrum results,  
321 the content of manganese increased with a higher Mn loading in membranes.



322

323 **Fig. 5.** EDS mapping image and spectrum of Mn-1/Al catalytic membrane (surface).

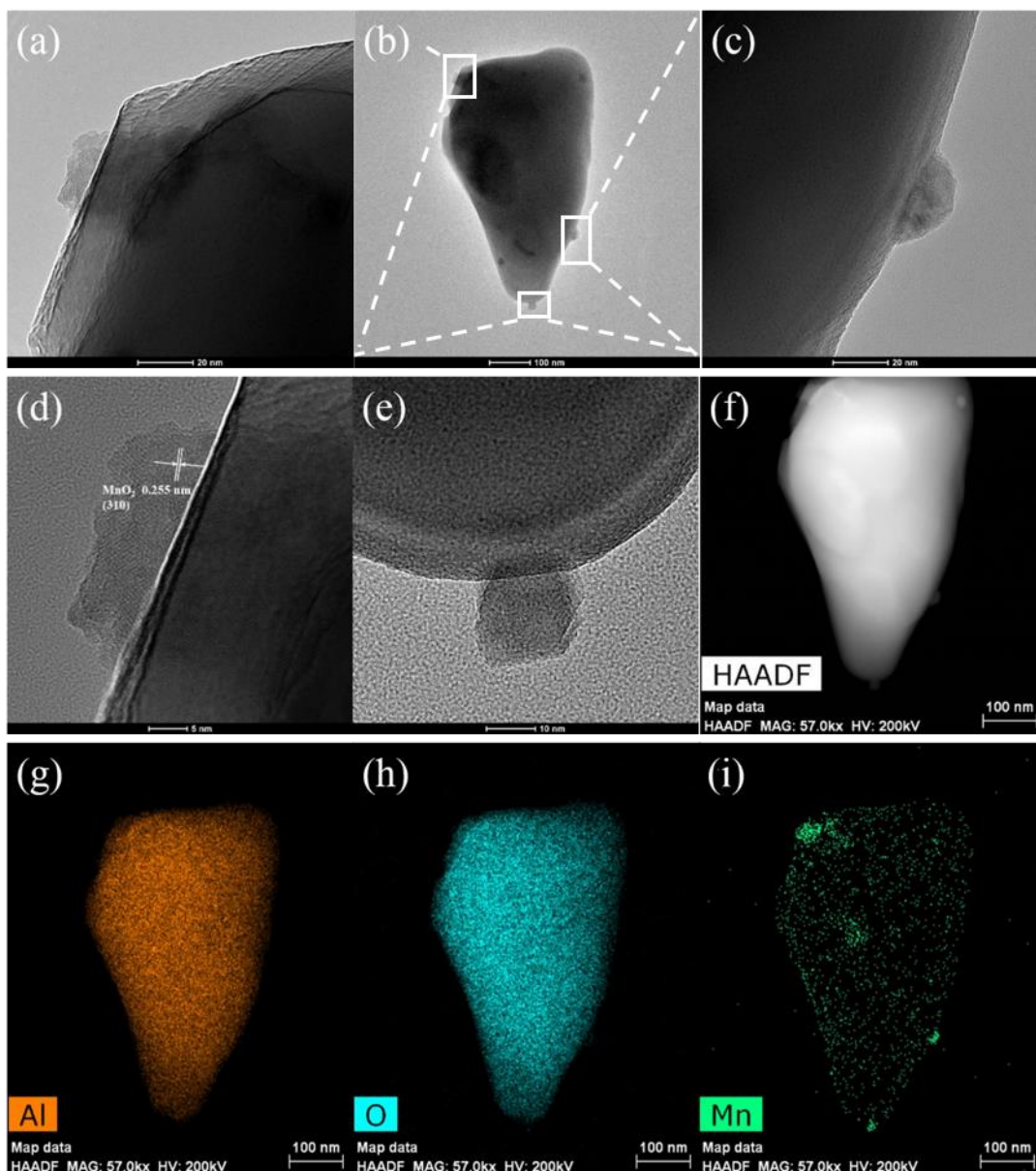


324

325 **Fig. 6.** EDS mapping image of Mn-3/Al catalytic membrane (cross-sectional).

326

327 Fig. 7 shows the HRTEM images and EDS mapping of a single  $\text{MnO}_2@ \text{Al}_2\text{O}_3$  particle from a  
 328 crushed powder of Mn-6/Al catalytic membrane. Fig.7b reveals three small  $\text{MnO}_2$   
 329 nanoparticles (10 - 20 nm) distributed dispersively on a  $\text{Al}_2\text{O}_3$  particle at the left top corner,  
 330 the right bottom corner, and the bottom corner, respectively. The zoom-in HRTEM images of  
 331 the three fine  $\text{MnO}_2$  particles are shown on Figs. 7 a, c and d. The 10-20 nm sized- $\text{MnO}_2$   
 332 particles half embedded into the 200-500 nm  $\text{Al}_2\text{O}_3$  particle. The fine dispersive  $\text{MnO}_2$  particles  
 333 on  $\text{Al}_2\text{O}_3$  can provide active sites for the catalytic oxidation process. In addition, the uniform  
 334 dispersion will enable evenly distributed flow of the fluid across the membrane, and efficient  
 335 interaction between  $\text{MnO}_2$  with PMS, which will lead to the high degradation rate of HBA. Fig.  
 336 7d reveals a lattice fringe with a distance of 2.55 Å, which is derived from the (310) crystal  
 337 plane of  $\text{MnO}_2$  (Ramsdellite, PDF# 72-1983).



338

339 **Fig. 7.** (a-e) HRTEM images, (f) HADFF, (g-i) elemental mapping of single  $\text{MnO}_2@Al_2O_3$   
 340 nanoparticles from membrane Mn-6/Al.

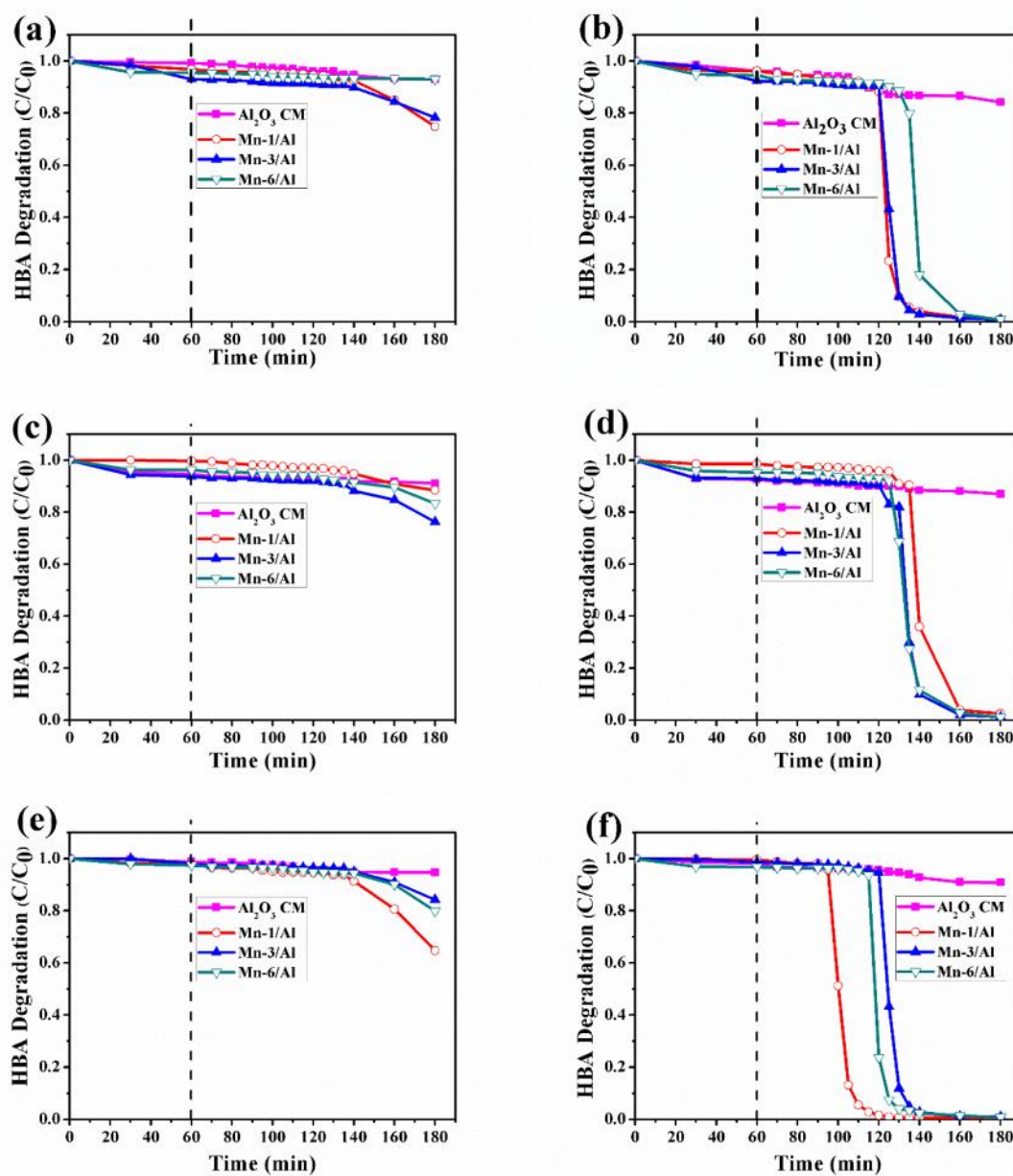
341

### 342 3.3. Catalytic oxidation of HBA

343 The catalytic activity of the ceramic, catalytic membranes for PMS activation was investigated  
 344 through the degradation of a typical antibiotics pollutant of 4-hydroxybenzoic acid (HBA)  
 345 (Criquet and Leitner 2015, (Tian et al. 2018)). Compared to the catalytic oxidation using  
 346 suspended catalysts, the  $\text{MnO}_2$ -incorporated catalytic membranes would avoid the recovery of

347 catalysts from the solution. Fig. 8 shows the effect of  $\text{MnO}_2$  loading on catalytic oxidation of  
348 HBA by the catalytic membranes. In all tests PMS was added at the time of 60 min. It was  
349 noticed that even at the permeate side, the catalytic oxidation reaction did not occur  
350 immediately. It normally experienced a concentration platform. This is because when the PMS  
351 was just added in the feed-in solution (Fig. 1), PMS needs time to be transported to the surface  
352 of membrane through tubing, because of the slow setting rate of peristaltic pump (around 0.2  
353 mL/min). The purpose of using a low feeding rate is to maintain the transmembrane pressure  
354 (TMP) at around 2 bar throughout the tests. The platform was not unanimous in every test that  
355 involves different catalytic membranes. This is because the actual pore size of different  
356 membranes changes with the loading of  $\text{MnO}_2$ , leading to the varied permeation resistance and  
357 subsequently varied velocity when the solution permeates through the membrane and flows in  
358 the system. However, the tendencies of HBA degradation were still very clear for each test. In  
359 this study, the catalyst loading amounts were 0.0167, 0.033, and 0.067 g of per gram  $\text{Al}_2\text{O}_3$  on  
360 Mn-1/Al, Mn-3/Al and Mn-6/Al, respectively. The weight of one ceramic membrane is 3.5 g.  
361 Taking Mn-1/Al catalytic membrane for example, there was 0.058 g  $\text{MnO}_2$  catalyst in the  
362 membrane. The solution used for catalytic oxidation was 500 mL, so the  $\text{MnO}_2$  catalysts  
363 loading in solution system can be equivalent to 0.1, 0.2 and 0.6 g/L, respectively. The former  
364 two catalysts loadings are common in SR-AOPs with suspended catalysts (Kang et al. 2016,  
365 Tian et al. 2018, (Wang et al. 2015a, (Yin et al. 2018). Figs. 8 a, c, and e show the HBA  
366 degradation at the feed-in side when initial HBA concentrations were at 20, 40, and 80 ppm,  
367 respectively. While Figs. 8 b, d, and f show the HBA concentrations on the permeate side. The  
368 pristine  $\text{Al}_2\text{O}_3$  ceramic membrane has minor performance on HBA degradation. A similar low  
369 performance was found on Mn-6 membrane without PMS on HBA degradation (Fig. S11).  
370 This is because that the HBA adsorption on membrane surface and within the membrane pores  
371 is negligible and the HBA degradation was caused by PMS itself (direct oxidation). With the

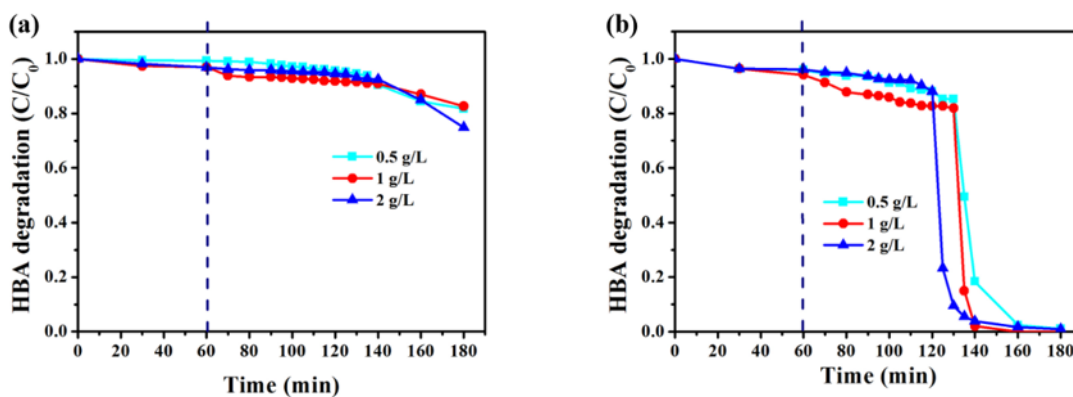
372 increase of MnO<sub>2</sub> loading amount, more catalytically active sites were provided for SO<sub>4</sub><sup>•-</sup>  
 373 generation from PMS activation. In a previous study, the organic pollutants degradation did  
 374 not show a big difference with increasing catalysts amount in catalytic membrane, which was  
 375 explained by mass transfer instead of radical generation (Bao et al. 2018). When compared  
 376 with the degradation results in other works (Wang et al. 2018, (Zhu et al. 2018), our  
 377 membranes showed a very good performance even at a high HBA initial concentration (80  
 378 ppm).



379

380 **Fig. 8.** Effect of initial HBA concentration on HBA degradation by different Mn loaded  
 381 catalytic membranes and unmodified membrane. (a) 20 ppm, feed-in side; (b) 20 ppm,  
 382 permeate side; (c) 40 ppm, feed-in side; (d) 40 ppm, permeate side, (e) 80 ppm, feed-in side,  
 383 and (f) 80 ppm, permeate side. PMS loading: 2 g/L; TMP: 2 bar; and temperature: 25 °C. PMS  
 384 was added at the time 60 min.

385  
 386 Figs. 9 (a) and (b) display the influence of PMS loading on HBA removal efficiency in the  
 387 range of 0.5 to 2 g/L. The HBA degradation at the permeate side (Fig. 9b) shows that the  
 388 oxidation reaction efficiency increased with the increase of PMS loading from 0.5 to 1 g/L.  
 389 However, a further increase of PMS loading to 2 g/L slightly reduced the overall oxidation  
 390 efficiency because of the self-quenching reaction with excess PMS. The effect of SR-AOPs  
 391 pretreatment was investigated and the results are shown in Fig. S12. In the pretreatment process,  
 392 PMS (2 g/L) and MnO<sub>2</sub> powders (0.2 g/L) were added in 100 mL HBA solution (20 ppm) and  
 393 stirred (200 rpm) for 10 min. Then the pretreatment solution was immediately added in the  
 394 dead-end filtration cell and the TMP was kept by nitrogen cylinder at 2 bar. At certain time  
 395 interval, 1 mL HBA solution was collected and the concentration was tested by HPLC. It was  
 396 found that the pretreatment process by MnO<sub>2</sub>/PMS cannot significantly degrade the HBA in a  
 397 120 min run. The 40 % degradation at the 5 min is due to the HBA degradation happened  
 398 outside the membrane cell (10 min stirring process). The 10 min equilibrium process can be  
 399 seen as a heterogeneous activation process by MnO<sub>2</sub> which leads to the most HBA degradation.



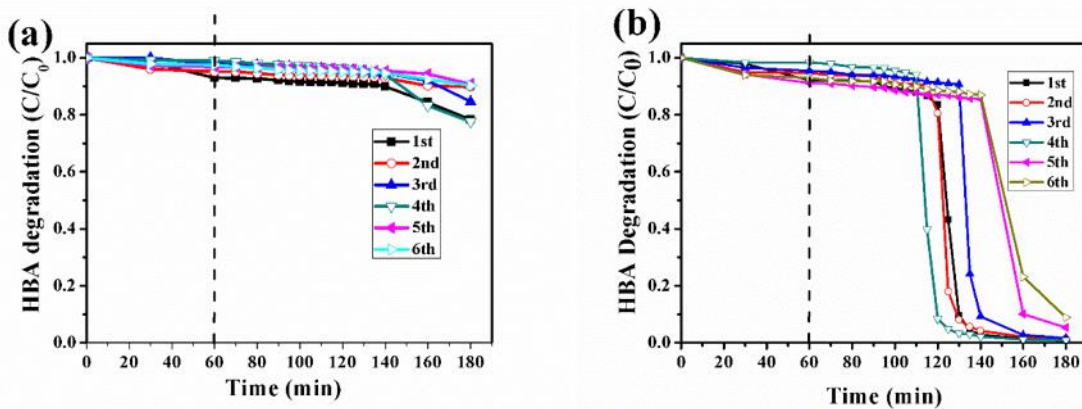
400

401 **Fig. 9.** Effect of initial PMS concentration on HBA degradation on Mn-1 membrane: (a) feed-  
402 in side; (b) permeate side. Initial HBA concentration: 20 ppm; TMP: 2 bar; and temperature:  
403 25 °C. PMS was added at the time 60 min.

404

405 The effect of SR-AOPs pretreatment was investigated and the results are shown in Fig. S12. In  
406 the pretreatment process, PMS (2 g/L) and MnO<sub>2</sub> powders (0.2 g/L) were added in 100 mL  
407 HBA solution (20 ppm) and stirred (200 rpm) for 10 min. Then the pretreatment solution was  
408 immediately added in the dead-end filtration cell and the TMP was kept by nitrogen cylinder  
409 at 1 bar. It was found that the pretreatment process by MnO<sub>2</sub>/PMS cannot significantly degrade  
410 the HBA in a 120 min run. The 40 % degradation at the 5 min is owing to the HBA degradation  
411 happened outside the membrane cell (10 min stirring process). The 10 min equilibrium process  
412 can be seen as a heterogeneous activation process by MnO<sub>2</sub> leading to the most HBA  
413 degradation.

414 The reusability tests of catalytic membrane were also investigated on Mn-3/Al membrane to  
415 treat 80 ppm HBA concentration in six runs (Fig. 10). The Mn-3/Al membrane was used  
416 directly without any post regeneration treatment but only being washed by ultrapure water and  
417 then dried in an oven overnight. The effectiveness of MnO<sub>2</sub> membrane did not decrease till the  
418 4<sup>th</sup> run. The degradation rate of 80 ppm HBA was still 100% at 180 min. At the 5<sup>th</sup> run and 6<sup>th</sup>  
419 run, the degradation rates decreased slightly for direct use, which were 95% and 91%,  
420 respectively. The robust and uniform structure of the ball-milling catalytic membrane provides  
421 a better stability than the other membranes reported recently (Wang et al. 2017a, (Wang et al.  
422 2018).



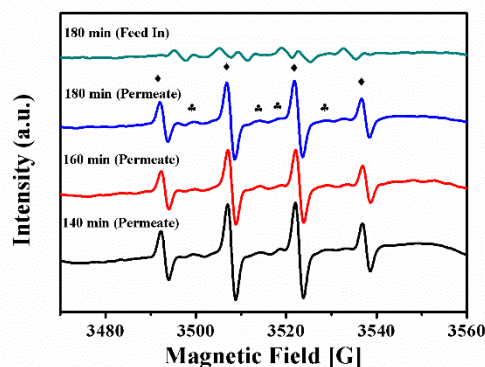
423

424 **Fig. 10.** Reusability tests of HBA degradation on Mn-3/Al catalytic membrane. (a) Feed-in  
 425 side; (b) Permeate side. HBA initial concentration: 80 ppm; PMS loading: 2 g/L; TMP: 2 bar;  
 426 and temperature: 25 °C. PMS was added at the 60 min.

427

#### 428 3.4. Mechanistic studies of HBA degradation in the MnO<sub>2</sub> CM/PMS system

429 It was reported that various reactive radicals such as SO<sub>4</sub><sup>•-</sup>, <sup>•</sup>OH, and O<sub>2</sub><sup>•-</sup> will be produced in  
 430 SR-AOPs system (Wang et al. 2017c). To identify the generation of reactive radicals as well  
 431 as the dominant radicals in the SR-AOPs facilitated by the catalytic membrane system, EPR  
 432 tests with DMPO as the spin trapping agent, were first performed. DMPO can react with  
 433 hydroxyl radicals and sulfate radicals, which can be revealed as the signals of DMPO-<sup>•</sup>OH and  
 434 DMPO- SO<sub>4</sub><sup>•-</sup> in Fig. 11. The EPR tests were performed in the membrane catalytic oxidation  
 435 of 20 ppm HBA by the Mn-3/Al membrane. Both SO<sub>4</sub><sup>•-</sup> and <sup>•</sup>OH were produced during the  
 436 PMS activation (Luo et al. 2018, (Ma et al. 2019). The signals from Feed-in side are much  
 437 weaker than that of permeate side, because the main reactions of radicals generation occur  
 438 when PMS interacts with MnO<sub>2</sub> in the pores of catalytic membrane.



439

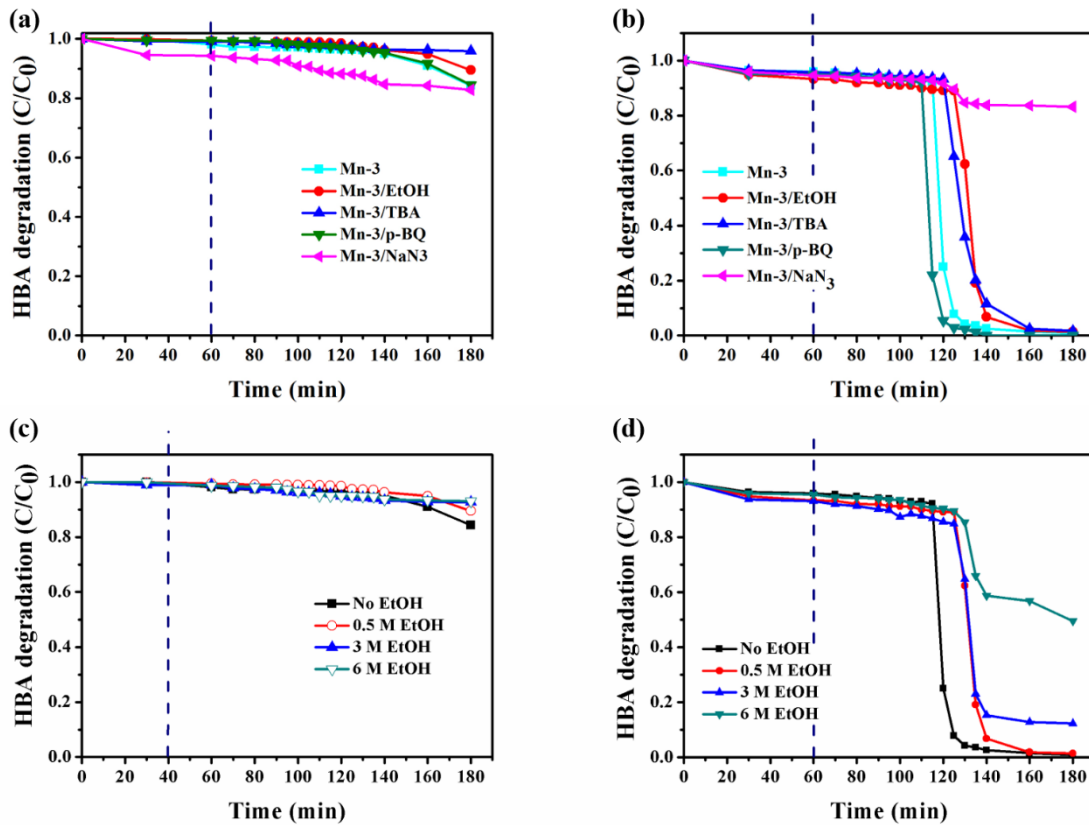
440 **Fig. 11.** EPR spectra for the Mn-3/Al sample. ((HBA)<sub>0</sub>: 20 ppm, PMS: 2 g/L, [T]: 25 °C; TMP:  
 441 2 bar; and pump rate: 0.2 mL/min. DMPO – ·OH ◆; DMPO – SO<sub>4</sub>·<sup>-</sup> ♣.

442

443 To probe the major radicals involved in the catalytic membrane system, ethanol (EtOH), tert-  
 444 butanol (TBA) and benzoquinone (p-BQ) were employed as the radical scavengers. EtOH is  
 445 effective to quench both hydroxyl radicals (rate constant of  $1.6 - 7.7 \times 10^7 \text{ M}^{-1}\text{s}^{-1}$ ) and sulfate  
 446 radicals (rate constant of  $1.2\text{-}2.8 \times 10^9 \text{ M}^{-1}\text{s}^{-1}$ ). TBA particularly works for the identification of  
 447 sulfate radicals because of the much larger rate constant with SO<sub>4</sub>·<sup>-</sup> ( $3.8 - 7.6 \times 10^9 \text{ M}^{-1}\text{s}^{-1}$ )  
 448 compared with that of ·OH ( $4.0 - 9.1 \times 10^5 \text{ M}^{-1}\text{s}^{-1}$ ) (Kang et al. 2019a). And p-BQ can be used  
 449 to identify superoxide radicals (O<sub>2</sub>·<sup>-</sup>) (rate constant =  $0.9 - 1 \times 10^9 \text{ M}^{-1}\text{s}^{-1}$ ). Fig. 12 shows the  
 450 quenching results on Mn-3/Al membrane. It was shown that SO<sub>4</sub>·<sup>-</sup> was the dominant radicals  
 451 in SR-AOPs using the catalytic membrane. Fig. 12 b shows that adding p-BQ has no significant  
 452 effect on HBA degradation, suggesting the absence of superoxide radicals. Both hydroxyl  
 453 radicals and sulfate radicals were proven to exist in this SR-AOPs catalytic membrane system,  
 454 owing to the decline of HBA oxidation efficiency at the permeate side.

455 Besides the reactive radicals oxidation pathway, non-radical oxidation pathway which relies  
 456 on singlet oxygen (<sup>1</sup>O<sub>2</sub>) was also an important reaction mechanism in SR-AOPs systems (Duan  
 457 et al. 2018c). It was found that with the addition of 40 mM NaN<sub>3</sub>, the HBA degradation at the  
 458 permeate side almost completely stopped. This finding is also consistent with a previous study

459 using metal oxides-coated ceramic membrane (CM) in Alcian Blue 8 GX dye removal (Zhao  
460 et al. 2019). However, as a strong reducing agent, sodium azide ( $\text{NaN}_3$ ) can react with not only  
461 singlet oxygen ( $^1\text{O}_2$ ) but hydroxyl and sulfate radicals (Duan et al. 2018c). The role of free  
462 radical pathway is then needed to be further investigated. Figs. 12c-d show the effect of ethanol  
463 concentration on HBA catalytic oxidation. At the permeate side (Fig. 12d), the 20 ppm HBA  
464 solution can be completely degraded in 180 min. The addition of 0.5 M ethanol can slightly  
465 suppress the generation of  $\text{SO}_4^{\bullet-}$  and  $\cdot\text{OH}$ , and still a HBA degradation efficiency of 98.6% can  
466 be achieved. When further increasing the ethanol concentration to 3 and 6 M, only 87.8 % and  
467 50.6% of HBA were decomposed in 180 min. In a previous study, ethanol was used as a radical  
468 scavenger in a  $\text{Co}_3\text{O}_4$  / PMS system. It was found when the ethanol to PMS ratio are 500:1  
469 (3.25 M of PMS) and 1000:1 (6.5 M of PMS), only around 40% and 20% of HBA degradation  
470 efficiency were achieved, respectively. And when the water was completely replaced by  
471 ethanol, no phenol degradation was observed (Duan et al. 2015b). Zhu et al. studied the  
472 mechanism of  $\beta\text{-MnO}_2$ /PS system and found that the sulfate and hydroxyl radicals were not  
473 produced. The singlet oxygen was generated and accounted for the phenol oxidation (Zhu et al.  
474 2019). Zhou et al. analysed the radical generation in  $\alpha\text{-MnO}_2$ /PMS and  $\delta\text{-MnO}_2$ /PMS systems.  
475 The results suggested that  $^1\text{O}_2$  and  $\text{O}_2^{\bullet-}$  have a little effect on the 4-NP (4-nitrophenol)  
476 degradation (Zhou et al. 2019). In conclusion, sulfate radicals ( $\text{SO}_4^{\bullet-}$ ), hydroxyl radicals ( $\cdot\text{OH}$ )  
477 and the non-radical degradation pathway exist in the Mn-catalytic membrane/PMS system, and  
478 no superoxide radicals ( $\text{O}_2^{\bullet-}$ ) produced. Free radical pathway dominated the reaction and  $\text{SO}_4^{\bullet-}$   
479  $^-$  plays a much more important role than  $\cdot\text{OH}$  in HBA degradation.



480

481 **Fig. 12.** Quenching tests for the Mn-3/Al sample. (a) Different quenching agent (feed-in side);  
 482 (b) Different quenching agent (permeate side) (TBA: 0.5 M, EtOH: 0.5 M, p-BQ: 2 mM, and  
 483  $\text{NaN}_3$ : 40 mM); (c) Different EtOH concentration quenching (feed-in side); and (d) Different  
 484 EtOH concentration quenching (Permeate side).  $(\text{HBA})_0$ : 20 PPM; PMS: 2 g/L;  $[T]$ : 25 °C;  
 485 TMP: 2 bar; and pump rate: 0.2 mL/min.

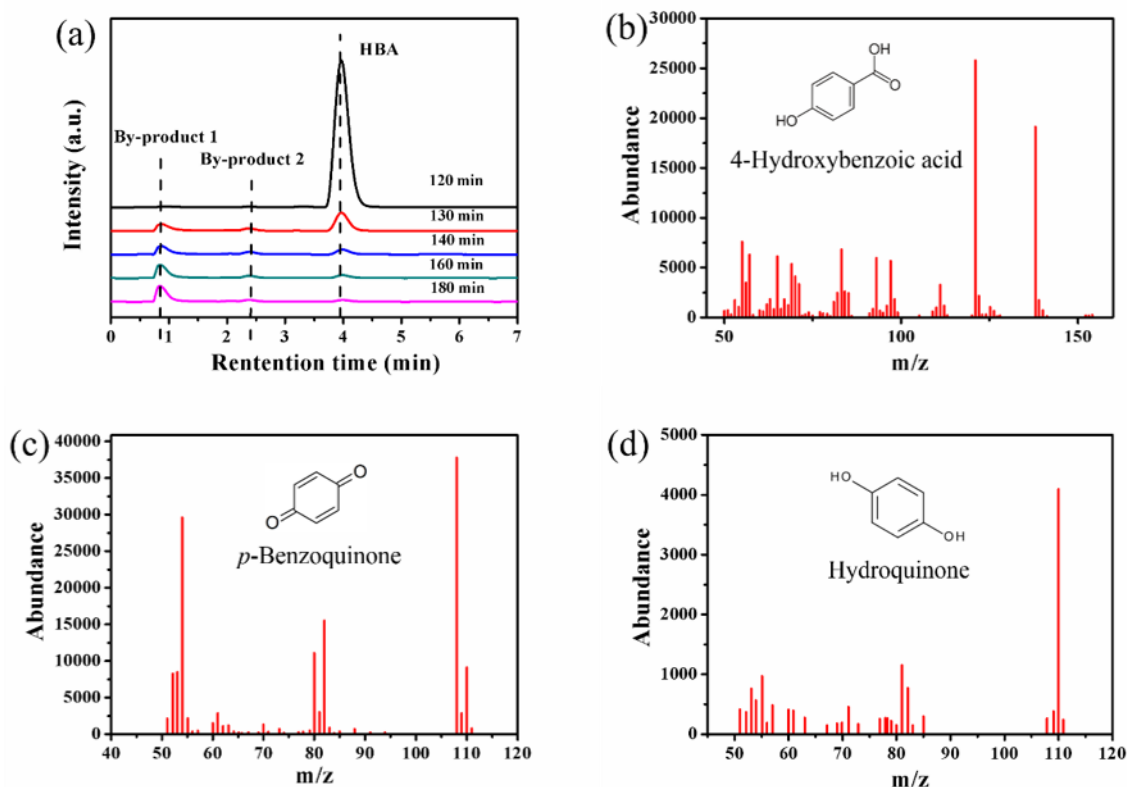
486

487 The manganese ions content was tested on ICP to verify Mn ion leaching. Samples from feed-  
 488 in tank of Mn-3/Al after the 1<sup>st</sup>, 4<sup>th</sup>, 5<sup>th</sup>, and 6<sup>th</sup> run of 20 ppm HBA degradation (the condition  
 489 is identical with Fig. 9 stability tests) are shown in Fig. S13. The Mn leaching of all the runs  
 490 were very low and the Mn ions in solution slightly increased with the test times. The Mn ions  
 491 content were in the order of 1<sup>st</sup> (1.16 mg/L) < 4<sup>th</sup> (1.69 mg/L) < 5<sup>th</sup> (1.99 mg/L) < 6<sup>th</sup> (2.82  
 492 mg/L).

493

494 3.5. HBA degradation pathways

495 In order to clarify the reaction pathway of the degradation of HBA over MnO<sub>2</sub> catalytic  
496 membrane in the presence of PMS, GC-MS analysis of the intermediates was carried out for  
497 the samples collected from permeate side on certain time interval (120, 130, 140, 160 and 180  
498 min). First, those solutions (1 mL solution without GC-MS extraction pretreatment steps) were  
499 injected into 1.5 mL UHPLC vials which pre-injected with 0.5 mL methanol as the quenching  
500 agent. The decay of HBA during the oxidation process monitored by UHPLC is illustrated in  
501 Fig. 13a.



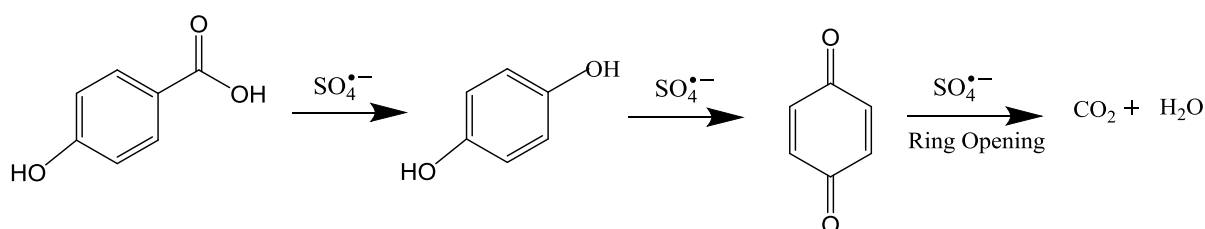
502

503 **Fig. 13.** (a) HPLC spectra of HBA degradation in a 180 min experiment. (Initial HBA  
504 concentration: 20 ppm, Mn-1/Al catalytic membrane, PMS concentration: 2 g/L, TMP: 2 bar);  
505 Mass spectra of (b) HBA, (c) p-Benzoquinone, and (d) Hydroquinone. (Initial HBA  
506 concentration: 20 ppm, Mn-3/Al catalytic membrane, PMS concentration: 2 g/L, and TMP set  
507 at 2 bar).

508

509 It can be seen that a well-defined HBA peak appeared at retention time ( $t_R$ ) = 3.98 min and the  
510 peak intensity gradually decreased while two major by-products were emerged during the  
511 oxidation process. GC-MS tests were carried out on the Agilent 7890B/5977B GC-MS system.  
512 The extract ion chromatography (EIC) signals of the HBA degradation intermediates were  
513 recorded with retention time between 0 – 28 min. When in the presence of  $\text{SO}_4^{\bullet-}$ , two by-  
514 products were confirmed: *p*-benzoquinone ( $m/z = 108.1$ ) and hydroquinone ( $m/z = 110.1$ ),  
515 during the HBA ( $m/z = 138.1$ ) oxidation process. The retention of *p*-benzoquinone (4.380 min)  
516 and hydroquinone (12.017 min) were shorter than that of HBA (15.618). The mass spectra of  
517 HBA, *p*-benzoquinone, and hydroquinone are shown in Figs. 13 b-d, respectively. Unlike  $\cdot\text{OH}$ ,  
518  $\text{SO}_4^{\bullet-}$  does not add to aromatic ring of HBA but directly reacts with HBA via electron transfer  
519 from the ring leading to the formation of a radical cation. The decarboxylation of the radical  
520 cation to HBA results in the formation of hydroquinone. Because the hydroquinone is easily to  
521 be oxidised, when in presence of  $\text{SO}_4^{\bullet-}$ , it will be further oxidised to *p*-benzoquinone.  
522 Subsequently, the  $\text{SO}_4^{\bullet-}$  can attack the C=C and C-C bond of *p*-benzoquinone, leading to the  
523 ring opening and formation of inorganic ions, carbon dioxide and water (Criquet and Leitner  
524 2015). The  $\text{SO}_4^{\bullet-}$  based HBA degradation pathway is shown in Fig. 14.

525



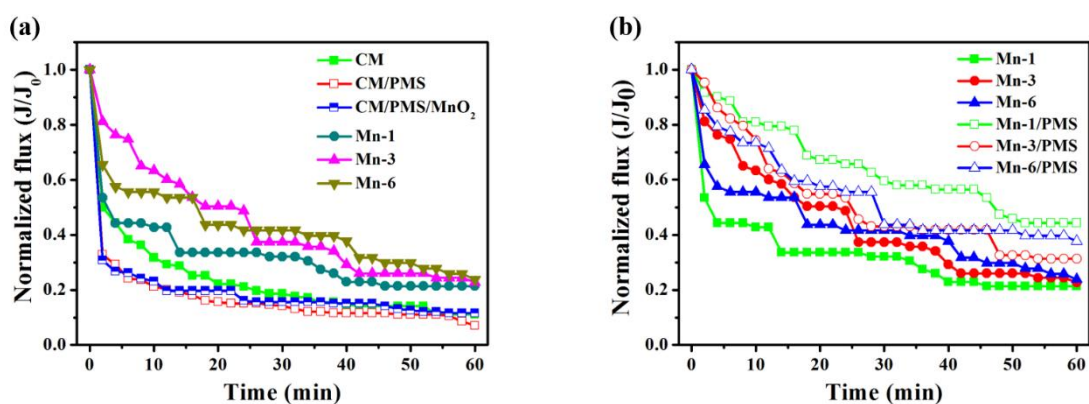
526

527 **Fig. 14.** Proposed degradation pathway of 4-hydroxybenzoic acid by  $\text{MnO}_2$  integrated catalytic  
528 membrane at the presence of PMS.

### 529 3.6. Membrane filtration performance

530 Fig. 15 shows the flux decline curves during the filtration of humic acids (HAs) by different  
531 membranes (CM, Mn-1, Mn-3, and Mn-6) under same parameters. For the CM, Mn-1, Mn-3,  
532 and Mn-6 samples, 100 mL HAs solution (2 g/L) was stirred for 30 min and then filtered  
533 through the dead-end filtration cell installed with the respective membrane (CM, Mn-1, Mn-3  
534 and Mn-6) under a pressure of 1 bar kept by the nitrogen cylinder. For the CM/PMS, Mn-1,  
535 Mn-3 and Mn-6 samples, the same amount HAs solution (2 g/L) mixed with PMS (4 g/L) was  
536 stirred for 1 h to reach a uniform dispersion of PMS within HAs solution, then filtered through  
537 the dead-end membrane cell. For the CM/PMS/MnO<sub>2</sub> system, the HAs solution (2 g/L) mixed  
538 with PMS (4 g/L) and MnO<sub>2</sub> (0.2 g/L) catalysts was stirred for 1 h to reach a uniform dispersion  
539 of PMS and MnO<sub>2</sub> within HAs solution, then filtered through the membrane cell which  
540 installed with the pure ceramic membrane (CM) under 1 bar pressure. The results showed that  
541 the flux decline of the pure ceramic membrane support (CM) is higher than that of Mn-1, Mn-  
542 3, and Mn-6 membrane, suggesting that the MnO<sub>2</sub> integrated ceramic membranes have a better  
543 fouling resistance compared with the pure alumina membrane support (Fig. 15a). When  
544 comparing with the permeate flux of CM, CM/PMS and CM/PMS/MnO<sub>2</sub>, it can be found that  
545 adding PMS or PMS and MnO<sub>2</sub> catalysts in HAs has no function in fouling alleviation when  
546 using pure ceramic membrane support (CM). The addition of PMS and MnO<sub>2</sub> even worsened  
547 the fouling condition. This can be ascribed to the fouling caused by MnO<sub>2</sub> nanoparticles and  
548 PMS (Fig. 15a). Fig. 15b shows the fouling alleviation performance of MnO<sub>2</sub> based catalytic  
549 membrane using PMS (4 g/L), The flux recovery happened in the MnO<sub>2</sub> based catalytic  
550 membranes with all loading (Mn-1, Mn-3 and Mn-6). It was found that the Mn-1/PMS sample  
551 has the best fouling recovery rate because of the relatively low flux resistance of the Mn-1  
552 membrane without PMS. A further increase of flux recovery rate from Mn-3/PMS to Mn-

553 6/PMS is because that the great increase of Mn loading leads to an improvement of anti-fouling  
554 performance.



555  
556 **Fig. 15.** Specific flux of different coated and uncoated membranes for filtration of humic acids  
557 (2 g/L). (a) pure ceramic supports and Mn catalytic membranes without PMS; (b) the  
558 comparative study of Mn catalytic membranes in flux change with or without PMS.

559

#### 560 4. Conclusions

561 In summary, catalytic ceramic membranes consisting of nano-structured MnO<sub>2</sub> dispersed  
562 uniformly inside the pores were prepared via a simple one-step ball-milling method for the first  
563 time. The ball-milling process not only contributes to the stable ceramic membrane formation,  
564 but helps the well-dispersive arrangement of fine MnO<sub>2</sub> catalysts on the surface of Al<sub>2</sub>O<sub>3</sub>  
565 particles. Different loading of MnO<sub>2</sub> catalytic membranes (1.67%, 3.33% and 6.67% of total  
566 membrane mass) were fabricated and the performance on HBA degradation were tested and  
567 compared. The uniform distribution of MnO<sub>2</sub> nanoparticles within the membrane pores and on  
568 the membrane surface provided sufficient active sites for PMS activation to generate SO<sub>4</sub><sup>•-</sup>,  
569 endowing the MnO<sub>2</sub> catalytic membrane with an excellent performance towards HBA catalytic  
570 oxidation even at a high initial HBA concentration (80 ppm) in a continuous cross-flow  
571 membrane device. It was found that the degradation efficiency slightly increased on a higher

572 loading, but even with the lowest loading (1.67% of MnO<sub>2</sub>) the effectiveness of HBA  
573 degradation was still high. This indicates the importance of membrane micro-structures for  
574 efficient utilisation of the MnO<sub>2</sub> catalyst. The stability and leaching tests revealed a good  
575 stability of the catalytic membrane even after the 6<sup>th</sup> run. EPR and quenching tests were applied  
576 to investigate the mechanism of PMS activation and HBA degradation. Both sulfate radicals  
577 (SO<sub>4</sub><sup>•-</sup>) and hydroxyl radicals (<sup>•</sup>OH) were generated in the catalytic membrane process. In  
578 addition, the non-radical pathway was also confirmed by NaN<sub>3</sub> and varying amount of ethanol  
579 quenching tests, but was not dominant for the degradation. Free radical pathway dominated the  
580 reaction and SO<sub>4</sub><sup>•-</sup> plays a much more important role than <sup>•</sup>OH in HBA degradation. HBA  
581 degradation intermediates were investigated by GC-MS, suggesting that hydroquinone and p-  
582 benzoquinone are the main intermediates. A possible HBA degradation route under the  
583 presence of SO<sub>4</sub><sup>•-</sup> was also proposed. This study provides a novel way for integrating  
584 membrane technology and AOPs towards practical water/wastewater treatments.

## 585 **Acknowledgements**

586 The author (Sun) would like to express his thanks for the supports from Vice-Chancellor's  
587 Professorial Research Fellowship. Both Z. Wu and H. Sun appreciate the support from  
588 IES\R3\170353 - International Exchanges 2017 Round 3. The authors acknowledge the help of  
589 M. Saunders, A. Suvorova, and L. Kirilak from the Centre for Microscopy, Characterization  
590 and Analysis (CMCA) of the University of Western Australia.

591

592

## 593 **References**

- 594 Anipsitakis, G.P. and Dionysiou, D.D., 2003. Degradation of organic contaminants in water  
595 with sulfate radicals generated by the conjunction of peroxymonosulfate with cobalt. *Environ.*  
596 *Sci. Technol.* 37(20), 4790-4797.
- 597 Anipsitakis, G.P. and Dionysiou, D.D., 2004a. Radical Generation by the Interaction of  
598 Transition Metals with Common Oxidants. *Environ. Sci. Technol.* 38(13), 3705-3712.
- 599 Anipsitakis, G.P. and Dionysiou, D.D., 2004b. Transition metal/UV-based advanced oxidation  
600 technologies for water decontamination. *Appl. Catal., B* 54(3), 155-163.
- 601 Bao, Y., Lim, T.-T., Wang, R., Webster, R.D. and Hu, X., 2018. Urea-assisted one-step  
602 synthesis of cobalt ferrite impregnated ceramic membrane for sulfamethoxazole degradation  
603 via peroxymonosulfate activation. *Chem. Eng. J.* 343, 737-747.
- 604 Chan, S.H.S., Yeong Wu, T., Juan, J.C. and Teh, C.Y., 2011. Recent developments of metal  
605 oxide semiconductors as photocatalysts in advanced oxidation processes (AOPs) for treatment  
606 of dye waste-water. *Journal of Chemical Technology & Biotechnology* 86(9), 1130-1158.
- 607 Chen, S., Yu, J., Wang, H., Yu, H. and Quan, X., 2015. A pilot-scale coupling catalytic  
608 ozonation–membrane filtration system for recirculating aquaculture wastewater treatment.  
609 *Desalination* 363(Supplement C), 37-43.
- 610 Cheng, X., Liang, H., Ding, A., Tang, X., Liu, B., Zhu, X., Gan, Z., Wu, D. and Li, G., 2017.  
611 Ferrous iron/peroxymonosulfate oxidation as a pretreatment for ceramic ultrafiltration  
612 membrane: Control of natural organic matter fouling and degradation of atrazine. *Water Res.*  
613 113, 32-41.
- 614 Cheng, X., Wu, D., Liang, H., Zhu, X., Tang, X., Gan, Z., Xing, J., Luo, X. and Li, G., 2018.  
615 Effect of sulfate radical-based oxidation pretreatments for mitigating ceramic UF membrane  
616 fouling caused by algal extracellular organic matter. *Water Res.* 145, 39-49.
- 617 Criquet, J. and Leitner, N.K.V., 2015. Reaction pathway of the degradation of the p-  
618 hydroxybenzoic acid by sulfate radical generated by ionizing radiations. *Radiat. Phys. Chem.*  
619 106, 307-314.
- 620 Duan, X., Ao, Z., Zhang, H., Saunders, M., Sun, H., Shao, Z. and Wang, S., 2018a.  
621 Nanodiamonds in sp<sup>2</sup>/sp<sup>3</sup> configuration for radical to nonradical oxidation: Core-shell layer  
622 dependence. *Appl. Catal., B* 222, 176-181.

623 Duan, X., Ao, Z., Zhou, L., Sun, H., Wang, G. and Wang, S., 2016a. Occurrence of radical and  
624 nonradical pathways from carbocatalysts for aqueous and nonaqueous catalytic oxidation. *Appl.*  
625 *Catal., B* 188, 98-105.

626 Duan, X., O'Donnell, K., Sun, H., Wang, Y. and Wang, S., 2015a. Sulfur and nitrogen co-  
627 doped graphene for metal-free catalytic oxidation reactions. *Small* 11(25), 3036-3044.

628 Duan, X., Su, C., Miao, J., Zhong, Y., Shao, Z., Wang, S. and Sun, H., 2018b. Insights into  
629 perovskite-catalyzed peroxymonosulfate activation: Maneuverable cobalt sites for promoted  
630 evolution of sulfate radicals. *Appl. Catal., B* 220, 626-634.

631 Duan, X., Sun, H., Ao, Z., Zhou, L., Wang, G. and Wang, S., 2016b. Unveiling the active sites  
632 of graphene-catalyzed peroxymonosulfate activation. *Carbon* 107, 371-378.

633 Duan, X., Sun, H., Shao, Z. and Wang, S., 2018c. Nonradical reactions in environmental  
634 remediation processes: Uncertainty and challenges. *Appl. Catal., B* 224, 973-982.

635 Duan, X., Sun, H., Tade, M. and Wang, S., 2018d. Metal-free activation of persulfate by cubic  
636 mesoporous carbons for catalytic oxidation via radical and nonradical processes. *Catal. Today*  
637 307, 140-146.

638 Duan, X., Sun, H., Wang, Y., Kang, J. and Wang, S., 2015b. N-Doping-induced nonradical  
639 reaction on single-walled carbon nanotubes for catalytic phenol oxidation. *ACS Catal.* 5(2),  
640 553-559.

641 Guo, Y., Xu, B. and Qi, F., 2016. A novel ceramic membrane coated with  $\text{MnO}_2\text{-Co}_3\text{O}_4$   
642 nanoparticles catalytic ozonation for benzophenone-3 degradation in aqueous solution:  
643 Fabrication, characterization and performance. *Chem. Eng. J.* 287(Supplement C), 381-389.

644 Kang, J., Duan, X., Zhou, L., Sun, H., Tade, M.O. and Wang, S., 2016. Carbocatalytic  
645 activation of persulfate for removal of antibiotics in water solutions. *Chem. Eng. J.* 288, 399-  
646 405.

647 Kang, J., Zhang, H., Duan, X., Sun, H., Tan, X., Liu, S. and Wang, S., 2019a. Magnetic Ni-Co  
648 alloy encapsulated N-doped carbon nanotubes for catalytic membrane degradation of emerging  
649 contaminants. *Chem. Eng. J.* 362, 251-261.

650 Kang, J., Zhou, L., Duan, X., Sun, H., Ao, Z. and Wang, S., 2019b. Degradation of cosmetic  
651 microplastics via functionalized carbon nanosprings. *Matter* 1, 745-758.

652 Kim, M., Hwang, Y. and Kim, J., 2013. Graphene/ $\text{MnO}_2$ -based composites reduced via  
653 different chemical agents for supercapacitors. *J. Power Sources* 239, 225-233.

654 Luo, X., Liang, H., Qu, F., Ding, A., Cheng, X., Tang, C.Y. and Li, G., 2018. Free-standing  
655 hierarchical  $\alpha\text{-MnO}_2\text{@CuO}$  membrane for catalytic filtration degradation of organic pollutants.  
656 *Chemosphere* 200, 237-247.

657 Ma, T., Liu, L., Meng, B., Gao, J., Wang, S. and Liu, S., 2019. Heterogeneous activation of  
658 peroxymonosulfate via a Ag-La<sub>0.8</sub>Ca<sub>0.2</sub>Fe<sub>0.94</sub>O<sub>3-δ</sub> perovskite hollow fibre membrane reactor for  
659 dye degradation. *Sep. Purif. Technol.* 211, 298-302.

660 Neyens, E. and Baeyens, J., 2003. A review of classic Fenton's peroxidation as an advanced  
661 oxidation technique. *J. Hazard. Mater.* 98(1-3), 33-50.

662 Norwood, W.P., Borgmann, U. and Dixon, D.G., 2007. Chronic toxicity of arsenic, cobalt,  
663 chromium and manganese to *Hyalella azteca* in relation to exposure and bioaccumulation.  
664 *Environ. Pollut.* 147(1), 262-272.

665 Saputra, E., Muhammad, S., Sun, H., Ang, H.-M., Tadó, M.O. and Wang, S., 2013a. A  
666 comparative study of spinel structured Mn<sub>3</sub>O<sub>4</sub>, Co<sub>3</sub>O<sub>4</sub> and Fe<sub>3</sub>O<sub>4</sub> nanoparticles in catalytic  
667 oxidation of phenolic contaminants in aqueous solutions. *J. Colloid Interface Sci.* 407, 467-  
668 473.

669 Saputra, E., Muhammad, S., Sun, H., Ang, H.-M., Tadó, M.O. and Wang, S., 2013b.  
670 Manganese oxides at different oxidation states for heterogeneous activation of  
671 peroxymonosulfate for phenol degradation in aqueous solutions. *Appl. Catal., B* 142, 729-735.

672 Saputra, E., Muhammad, S., Sun, H., Ang, H.M., Tade, M. and Wang, S., 2013c. Different  
673 crystallographic one-dimensional MnO<sub>2</sub> nanomaterials and their superior performance in  
674 catalytic phenol degradation. *Environ. Sci. Technol.* 47(11), 5882-5887.

675 Sun, H., Kwan, C., Suvorova, A., Ang, H.M., Tadó, M.O. and Wang, S., 2014. Catalytic  
676 oxidation of organic pollutants on pristine and surface nitrogen-modified carbon nanotubes  
677 with sulfate radicals. *Appl. Catal., B* 154-155, 134-141.

678 Sun, H. and Wang, S., 2015. Catalytic oxidation of organic pollutants in aqueous solution using  
679 sulfate radicals. *Catalysis* 27, 209-247.

680 Sun, H., Zhou, G., Liu, S., Ang, H.M., Tadó, M.O. and Wang, S., 2012. Nano-Fe<sup>0</sup> encapsulated  
681 in microcarbon spheres: Synthesis, characterization, and environmental applications. *ACS*  
682 *Appl. Mater. Interfaces* 4(11), 6235-6241.

683 Tian, W., Zhang, H., Qian, Z., Ouyang, T., Sun, H., Qin, J., Tadó, M.O. and Wang, S., 2018.  
684 Bread-making synthesis of hierarchically Co@C nanoarchitecture in heteroatom doped porous  
685 carbons for oxidative degradation of emerging contaminants. *Appl. Catal., B* 225, 76-83.

686 Wang, G., Wang, D., Dong, X., Zhang, X. and Ma, H., 2017a. Sodium persulfate based PVDF  
687 membrane for concurrent advanced oxidation and ultrafiltration of ofloxacin in water. *Chem.*  
688 *Eng. J.* 315, 509-515.

689 Wang, J.-G., Yang, Y., Huang, Z.-H. and Kang, F., 2013. A high-performance asymmetric  
690 supercapacitor based on carbon and carbon-MnO<sub>2</sub> nanofiber electrodes. *Carbon* 61, 190-199.

691 Wang, W., Wang, H., Li, G., An, T., Zhao, H. and Wong, P.K., 2019. Catalyst-free activation  
692 of persulfate by visible light for water disinfection: Efficiency and mechanisms. *Water Res.*  
693 157, 106-118.

694 Wang, X., Wang, G., Chen, S., Fan, X., Quan, X. and Yu, H., 2017b. Integration of membrane  
695 filtration and photoelectrocatalysis on g-C<sub>3</sub>N<sub>4</sub>/CNTs/Al<sub>2</sub>O<sub>3</sub> membrane with visible-light  
696 response for enhanced water treatment. *J. Membr. Sci.* 541(Supplement C), 153-161.

697 Wang, Y., Cao, D., Liu, M. and Zhao, X., 2017c. Insights into heterogeneous catalytic  
698 activation of peroxydisulfate by Pd/g-C<sub>3</sub>N<sub>4</sub>: The role of superoxide radical and singlet  
699 oxygen. *Catal. Commun.* 102, 85-88.

700 Wang, Y., Sun, H., Ang, H.M., Tadó, M.O. and Wang, S., 2015a. 3D-hierarchically structured  
701 MnO<sub>2</sub> for catalytic oxidation of phenol solutions by activation of peroxydisulfate: Structure  
702 dependence and mechanism. *Appl. Catal., B* 164, 159-167.

703 Wang, Y., Sun, H., Duan, X., Ang, H.M., Tadó, M.O. and Wang, S., 2015b. A new magnetic  
704 nano zero-valent iron encapsulated in carbon spheres for oxidative degradation of phenol. *Appl.*  
705 *Catal., B* 172–173, 73-81.

706 Wang, Y., Zhao, S., Fan, W., Tian, Y. and Zhao, X., 2018. The synthesis of novel Co–Al<sub>2</sub>O<sub>3</sub>  
707 nanofibrous membranes with efficient activation of peroxydisulfate for bisphenol A  
708 degradation. *Environ. Sci.: Nano* 5(8), 1933-1942.

709 Wang, Y., Zhou, L., Duan, X., Sun, H., Tin, E.L., Jin, W. and Wang, S., 2015c. Photochemical  
710 degradation of phenol solutions on Co<sub>3</sub>O<sub>4</sub> nanorods with sulfate radicals. *Catal. Today* 258(Part  
711 2), 576-584.

712 Xia, D., Yin, R., Sun, J., An, T., Li, G., Wang, W., Zhao, H. and Wong, P.K., 2017. Natural  
713 magnetic pyrrhotite as a high-Efficient persulfate activator for micropollutants degradation:  
714 Radicals identification and toxicity evaluation. *J. Hazard. Mater.* 340, 435-444.

715 Xiao, K., Li, J.-W., Chen, G.-F., Liu, Z.-Q., Li, N. and Su, Y.-Z., 2014. Amorphous MnO<sub>2</sub>  
716 supported on 3D-Ni nanodendrites for large areal capacitance supercapacitors. *Electrochim.*  
717 *Acta* 149, 341-348.

718 Yin, Y., Shi, L., Li, W., Li, X., Wu, H., Ao, Z., Tian, W., Liu, S., Wang, S. and Sun, H., 2019.  
719 Boosting Fenton-like reactions via single atom Fe catalysis. *Environ. Sci. Technol.* in press  
720 (DOI: 10.1021/acs.est.9b03342).

721 Yin, Y., Wu, H., Shi, L., Zhang, J., Xu, X., Zhang, H., Wang, S., Sillanpää, M. and Sun, H.,  
722 2018. Quasi single cobalt sites in nanopores for superior catalytic oxidation of organic  
723 pollutants. *Environ. Sci.: Nano* 5(12), 2842-2852.

724 Zhao, H., Chen, S., Quan, X., Yu, H. and Zhao, H., 2016. Integration of microfiltration and  
725 visible-light-driven photocatalysis on g-C<sub>3</sub>N<sub>4</sub> nanosheet/reduced graphene oxide membrane for  
726 enhanced water treatment. *Appl. Catal., B* 194, 134-140.

727 Zhao, Q., Lu, D., Jiang, H., Zhao, Y., Sun, Y., Li, Z., Yang, M., Wang, P. and Ma, J., 2019.  
728 Peroxymonosulfate-based cleaning technology for metal oxide-coated ceramic ultrafiltration  
729 membrane polluted by Alcian Blue 8GX dye: Radical and non-radical oxidation cleaning  
730 mechanism. *J. Membr. Sci.* 573, 210-217.

731 Zhou, Z.-G., Du, H.-M., Dai, Z., Mu, Y., Tong, L.-L., Xing, Q.-J., Liu, S.-S., Ao, Z. and Zou,  
732 J.-P., 2019. Degradation of organic pollutants by peroxymonosulfate activated by MnO<sub>2</sub> with  
733 different crystalline structures: Catalytic performances and mechanisms. *Chem. Eng. J.* 374,  
734 170-180.

735 Zhu, S., Li, X., Kang, J., Duan, X. and Wang, S., 2019. Persulfate activation on crystallographic  
736 manganese oxides: Mechanism of singlet oxygen evolution for nonradical selective  
737 degradation of aqueous contaminants. *Environ. Sci. Technol.* 53, 307-315.

738 Zhu, Z.-S., Qu, J., Hao, S.-M., Han, S., Jia, K.-L. and Yu, Z.-Z., 2018.  $\alpha$ -Fe<sub>2</sub>O<sub>3</sub>  
739 Nanodisk/bacterial cellulose hybrid membranes as high-performance sulfate-radical-based  
740 visible light photocatalysts under stirring/flowing states. *ACS Appl. Mater. Interfaces* 10,  
741 30670-30679.

742